Mon. Not. R. Astron. Soc. **396,** 2295–2312 (2009) doi:10.1111/j.1365-2966.2009.14898.x

On the derivation of dynamical masses of the stellar clusters in the circumnuclear region of NGC 2903

Guillermo F. Hägele,[1,2]★ Ángeles I. Díaz,[1] Mónica V. Cardaci,[1,3]† Elena Terlevich[4]‡ and Roberto Terlevich[4]‡

[1]*Departamento de Física Teórica, C-XI, Universidad Autónoma de Madrid, 28049 Madrid, Spain*
[2]*Facultad de Cs Astronómicas y Geofísicas, Universidad Nacional de La Plata, Paseo del Bosque s/n, 1900 La Plata, Argentina*
[3]*XMM Science Operations Centre, European Space Astronomy Centre of ESA, PO Box 50727, 28080 Madrid, Spain*
[4]*INAOE, Tonantzintla, Apdo. Postal 51, 72000 Puebla, México*

Accepted 2009 April 8. Received 2009 April 7; in original form 2008 November 4

ABSTRACT

Gas and star velocity dispersions have been derived for four circumnuclear star-forming regions (CNSFRs) and the nucleus of the spiral galaxy NGC 2903 using high-resolution spectroscopy in the blue and far red. Stellar velocity dispersions have been obtained from the Ca II triplet lines at λλ 8494, 8542, 8662 Å, using cross-correlation techniques, while gas velocity dispersions have been measured by Gaussian fits to the Hβ λ 4861 Å line.

The CNSFRs, with sizes of about 100 to 150 pc in diameter, show a complex structure at the *Hubble Space Telescope* (*HST*) resolution, with a good number of subclusters with linear diameters between 3 and 8 pc. Their stellar velocity dispersions range from 39 to 67 km s^{-1}. These values, together with the sizes measured on archival *HST* images, yield upper limits to the dynamical masses for the individual star clusters between 1.8 and 8.7 × 10^6 M$_\odot$ and upper limits to the masses for the whole CNSFR between 4.9 × 10^6 and 4.3 × 10^7 M$_\odot$.

The masses of the ionizing stellar population responsible for the H II region gaseous emission have been derived from their published Hα luminosities and are found to be between 1.9 and 2.5 × 10^6 M$_\odot$ for the star-forming regions, and 2.1 × 10^5 M$_\odot$ for the galaxy nucleus, therefore constituting between 1 and 4 per cent of the total dynamical mass.

In the CNSFR, star and gas velocity dispersions are found to differ by about 20 km s^{-1} with the Hβ lines being narrower than both the stellar lines and the [O III] λ 5007 Å lines. The ionized gas kinematics are complex; two different kinematical components seem to be present as evidenced by different widths and Doppler shifts.

The line profiles in the spectra of the galaxy nucleus, however, are consistent with the presence of a single component with radial velocity and velocity dispersion close to those measured for the stellar absorption lines.

The presence and reach of two distinct components in the emission lines in ionized regions and the influence that this fact could have on the observed line ratios are of major interest for several reasons, among others, the classification of the activity in the central regions of galaxies, the inferences about the nature of the source of ionization for the two components and the derivation of the gaseous chemical abundances.

Key words: H II regions – galaxies: individual: NGC 2903 – galaxies: kinematics and dynamics – galaxies: starburst – galaxies: star clusters.

1 INTRODUCTION

The inner (∼1 kpc) parts of some spiral galaxies show high star formation rates, and this star formation is frequently arranged in a ring or pseudo-ring pattern around their nuclei. This fact seems to correlate with the presence of bars (Roberts, Huntley & van Albada 1979; Friedli & Benz 1995; Sakamoto et al. 1999; Jogee, Scoville

★E-mail: guille.hagele@uam.es
†PhD fellow of Ministerio de Educación y Ciencia, Spain.
‡Research affiliate at IoA.

& Kenney 2005; Sheth et al. 2005) and, in fact, computer models which simulate the behaviour of gas in galactic potentials have shown that nuclear rings may appear as a consequence of matter infall owing to resonances present at the bar edges (Combes & Gerin 1985; Athanassoula 1992).

These circumnuclear star-forming regions (CNSFRs) are expected to be amongst the highest metallicity regions as corresponds to their position near the galactic centre. This fact makes the analysis of these regions complicated since, in general, their low excitation makes any temperature-sensitive line too weak to be measured (Díaz et al. 2007), particularly against a strong underlying stellar continuum. As was pointed out in Hägele et al. (2007) (hereafter Paper I), the [O III] emission lines in CNSFRs are generally very weak, and in some cases unobservable. The low value of these collisionally excited lines can be explained by their over-solar metal abundances (e.g. Boer & Schulz 1993). The equivalent width (EW) of the emission lines is lower than those shown by the disc H II regions (see e.g. Kennicutt, Keel & Blaha 1989; Bresolin & Kennicutt 1997; Bresolin, Kennicutt & Garnett 1999). Combining GEMINI data and a grid of photoionization models, Dors et al. (2008) conclude that the contamination of the continua of CNSFRs by underlying contributions from both old bulge stars and stars formed in the ring in previous episodes of star formation (10–20 Myr) yields the observed low EWs.

CNSFRs, with sizes going from a few tens to a few hundreds of parsecs (e.g. Díaz et al. 2000a), seem to be made of several H II regions ionized by luminous compact stellar clusters whose sizes, as measured from high spatial resolution *Hubble Space Telescope* (*HST*) images, are seen to be of only a few parsecs. Although these H II regions are very luminous (M_v between -12 and -17), not much is known about their kinematics or dynamics for both the ionized gas and the stars. It could be said that the worst known parameter of these ionizing clusters is their mass. There are different methods to estimate the mass of a stellar cluster. As derived with the use of population synthesis models, their masses suggest that these clusters are gravitationally bound and that they might evolve into globular cluster configurations (Maoz et al. 1996). Classically one assumes that the system is virialized and determines the total mass inside a radius by applying the virial theorem to the observed velocity dispersion of the stars (σ_*). The stellar velocity dispersion is however hard to measure in young stellar clusters (a few million years old) due to the shortage of prominent stellar absorption lines. The optical continuum between 3500 and 7000 Å shows very few lines since the light at these wavelengths is dominated by OB stars which have weak absorption lines at the same wavelengths of the nebular emission lines (Balmer H and He I lines). As pointed out by several authors (e.g. Ho & Filippenko 1996a), at longer wavelengths (8500 Å) the contamination due to nebular lines is much smaller and since red supergiant stars, if present, dominate the near-infrared (NIR) light where the Ca II λλ 8498, 8542, 8662 Å triplet (CaT) lines are found, these should be easily observable allowing the determination of σ_* (Terlevich et al. 1990; Prada, Greve & McKeith 1994).

NGC 2903 (UGC 5079) is a well-studied galaxy classified as a SB(rs)bc by de Vaucouleurs et al. (1991). Its coordinates are $\alpha_{2000} = 09^{\rm h}\,32^{\rm m}\,10\overset{\rm s}{.}1$, $\delta_{2000} = +21^\circ\,30'\,03''$ (de Vaucouleurs et al. 1991). These authors derived a B_T (mag) equal to 9.7 and an $E(B-V)_{\rm gal}$ (mag) of 0.031. We adopt the distance derived by Bottinelli et al. (1984) which is equal to 8.6 Mpc, giving a linear scale of ∼42 pc arcsec^{-1}.

The Paschen α image obtained with the *HST* reveals in NGC 2903 the presence of a nuclear ring-like morphology with an apparent diameter of approximately 15 arcsec = 625 pc (Alonso-Herrero, Ryder & Knapen 2001). This structure is also seen, though less prominent, in the Hα observations from Planesas, Colina & Pérez-Olea (1997). A large number of stellar clusters are identified on high-resolution IR images in the K' and H bands, which do not coincide spatially with the bright H II regions. A possible interpretation of this is that the stellar clusters are the result of the evolution of giant H II regions (e.g. Alonso-Herrero et al. 2001). The global star formation rates in the nuclear ring, as derived from its Hα luminosity, are found to be 0.1 $M_\odot$ yr^{-1} by Planesas et al. (1997) and 0.7 $M_\odot$ yr^{-1} by Alonso-Herrero et al. (2001). From CO emission observations, Planesas et al. derive a mass of molecular gas (H_2) of 1.8×10^8 $M_\odot$ inside a circle 1 kpc in diameter.

This is the second paper of a series to study the peculiar conditions of star formation in circumnuclear regions of early-type spiral galaxies, in particular the kinematics of the connected stars and gas. In this paper, we present high-resolution far-red spectra and stellar velocity dispersion measurements (σ_*) along the line of sight for four CNSFRs and the nucleus of the spiral galaxy NGC 2903. We have also measured the ionized gas velocity dispersions ($\sigma_{\rm g}$) from high-resolution blue spectra using Balmer Hβ and [O III] emission lines. The comparison between σ_* and $\sigma_{\rm g}$ might throw some light on the yet unsolved issue about the validity of the gravitational hypothesis for the origin of the supersonic motions observed in the ionized gas in Giant H II regions (Melnick, Tenorio-Tagle & Terlevich 1999).

In Section 2, we describe the observations and data reduction. We present the results in Section 3, the dynamical mass derivation in Section 4 and the ionizing star cluster properties in Section 5. We discuss all our results in Section 6. Finally, summary and conclusions are given in Section 7.

2 OBSERVATIONS AND DATA REDUCTION

The data were acquired in 2000 February using the two arms of the ISIS spectrograph attached to the 4.2-m William Herschel Telescope (WHT) of the Isaac Newton Group (ING) at the Roque de los Muchachos Observatory on the Spanish island of La Palma. The CCD detectors EEV12 and TEK4 were used for the blue and red arms with a factor of 2 binning in both the 'x' and 'y' directions with resultant spatial resolutions of 0.38 and 0.36 arcsec pixel^{-1} for the blue and red configurations, respectively. The H2400B and R1200R gratings were used to cover the wavelength ranges from 4779 to 5199 Å ($\lambda_{\rm c} = 4989$ Å) in the blue and from 8363 to 8763 Å ($\lambda_{\rm c} = 8563$ Å) in the red with resultant spectral dispersions of 0.21 and 0.39 Å pixel^{-1}, respectively, providing a comparable velocity resolution of about 13 km s^{-1}. A slit width of 1 arcsec was used which, combined with the spectral dispersions, yielded spectral resolutions of about 0.4 and 0.7 Å full width at half-maximum (FWHM) in the blue and the red, respectively, measured on the sky lines. Table 1 summarizes the instrumental configuration and observation details. Several bias and sky flat-field frames were taken at the beginning and end of each night in both arms. In addition, two lamp flat-field and one-calibration lamp exposures per telescope position were performed. The calibration lamp used was CuNe+CuAr.

The data were processed and analysed using IRAF[1] routines including the usual procedures of removal of cosmic rays, bias subtraction,

[1] IRAF: the Image Reduction and Analysis Facility is distributed by the National Optical Astronomy Observatories, which is operated by the Association of Universities for Research in Astronomy, Inc. (AURA) under cooperative agreement with the National Science Foundation.

Table 1. Journal of observations.

Date	Spectral range (Å)	Disp. (Å pixel^{-1})	$R^{a}_{\rm FWHM}$	Spatial res. (arcsec pixel^{-1})	PA (°)	Exposure time (s)	Seeing$_{\rm FWHM}$ (arcsec)
2000 February 4	4779–5199	0.21	~12 500	0.38	50	3 × 1200	1.2
	8363–8763	0.39	~12 200	0.36	50	3 × 1200	
2000 February 5	4779–5199	0.21	~12 500	0.38	345	3 × 1200	1.6
	8363–8763	0.39	~12 200	0.36	345	3 × 1200	

[a] $R_{\rm FWHM} = \lambda/\Delta\lambda_{\rm FWHM}$.

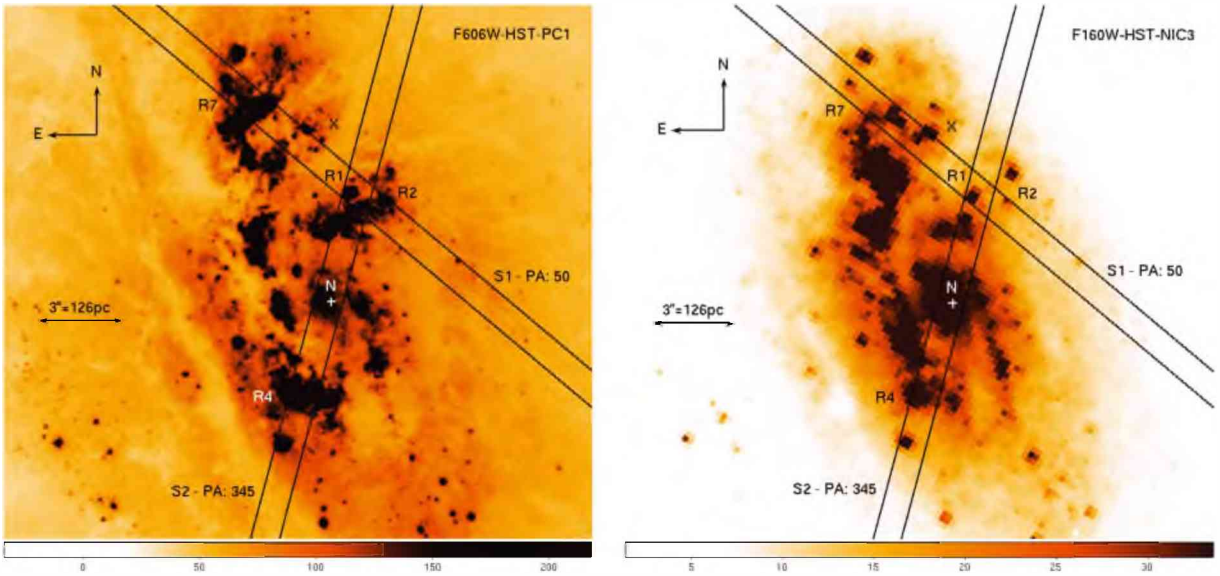

Figure 1. Left-hand panel: F606W (wide *V*) image centred on NGC 2903 obtained with the WFPC2 camera (PC1) of the *HST*. Right-hand panel: *HST*–NICMOS (NIC3) image obtained through the F160W filter. For both images, the orientation is north up, east to the left. The location and position angle (PA) of the WHT–ISIS slit positions, together with identifications of the CNSFRs extracted, are marked.

division by a normalized flat-field and wavelength calibration. Further details concerning each of these steps can be found in Paper I.

Neither atmospheric extinction nor flux calibration was performed, since our purpose was to measure radial velocities and velocity dispersions. With this purpose, spectra of 11 template velocity stars were acquired to provide good stellar reference frames in the same system as the galaxy spectra for the kinematic analysis in the far red. They correspond to late-type giant and supergiant stars which have strong CaT features (see Díaz, Terlevich & Terlevich 1989). The spectral types, luminosity classes and dates of observation of the stellar reference frames used as templates are listed in table 2 of Paper I.

3 RESULTS

Two different slit positions (S1 and S2) were chosen in order to observe the nucleus of the galaxy and four CNSFRs. Fig. 1 shows them superimposed on photometrically calibrated optical and IR images of the circumnuclear region of NGC 2903 acquired with the Wide Field Planetary Camera 2 (WFPC2; PC1) and the Near-Infrared Camera and Multi-Object Spectrometer (NICMOS) Camera 3 (NIC3) on board the *HST*. These images have been downloaded from the Multimission Archive at STScI [Multimission Archive at the Space Telescope Science Institute (MAST)].[2] The optical image was obtained through the F606W (wide *V*) filter, and the NIR one, through the F160W (H). The CNSFRs have been labelled following the same nomenclature as in Planesas et al. (1997) from their identifications on Hα maps. The plus symbol in both panels of Fig. 1 represents the position of the nucleus as given by the Two-Micron All-Sky Survey (2MASS) Team, 2MASS Extended Ojects – Final Release (Jarrett et al. 2003).

Fig. 2 shows the spatial profiles in the Hβ and [O III] 5007 Å emission lines (upper and middle panels) and the far-red continuum (lower panels) along each slit position. The emission line profiles have been generated by collapsing 11 pixels of the spectra in the direction of the resolution at the central position of the lines in the rest frame, λ 4861 and λ 5007 Å, respectively, and are plotted as dashed lines. Continuum profiles were generated by collapsing 11 resolution pixels centred at 11 Å to the blue of each emission line and are plotted as dash–dotted lines. The difference between the two, shown by solid lines, corresponds to the pure emission. The far-red continuum has been generated by collapsing 11 pixels centred at λ 8620Å.

The regions of the frames to be extracted into one-dimensional spectra corresponding to each of the identified CNSFRs were selected on these profiles with reference to the continuum emission both in the blue and in the red. These regions are marked by horizontal lines and labelled in the figure. In the Hβ profile of slit position S1, an almost pure emission knot between regions R1+R2 and R7 can be seen with a very weak continuum. We labelled this region as X. In the case of the [O III] 5007 Å emission line profile, the main

[2] http://archive.stsci.edu/hst/wfpc2

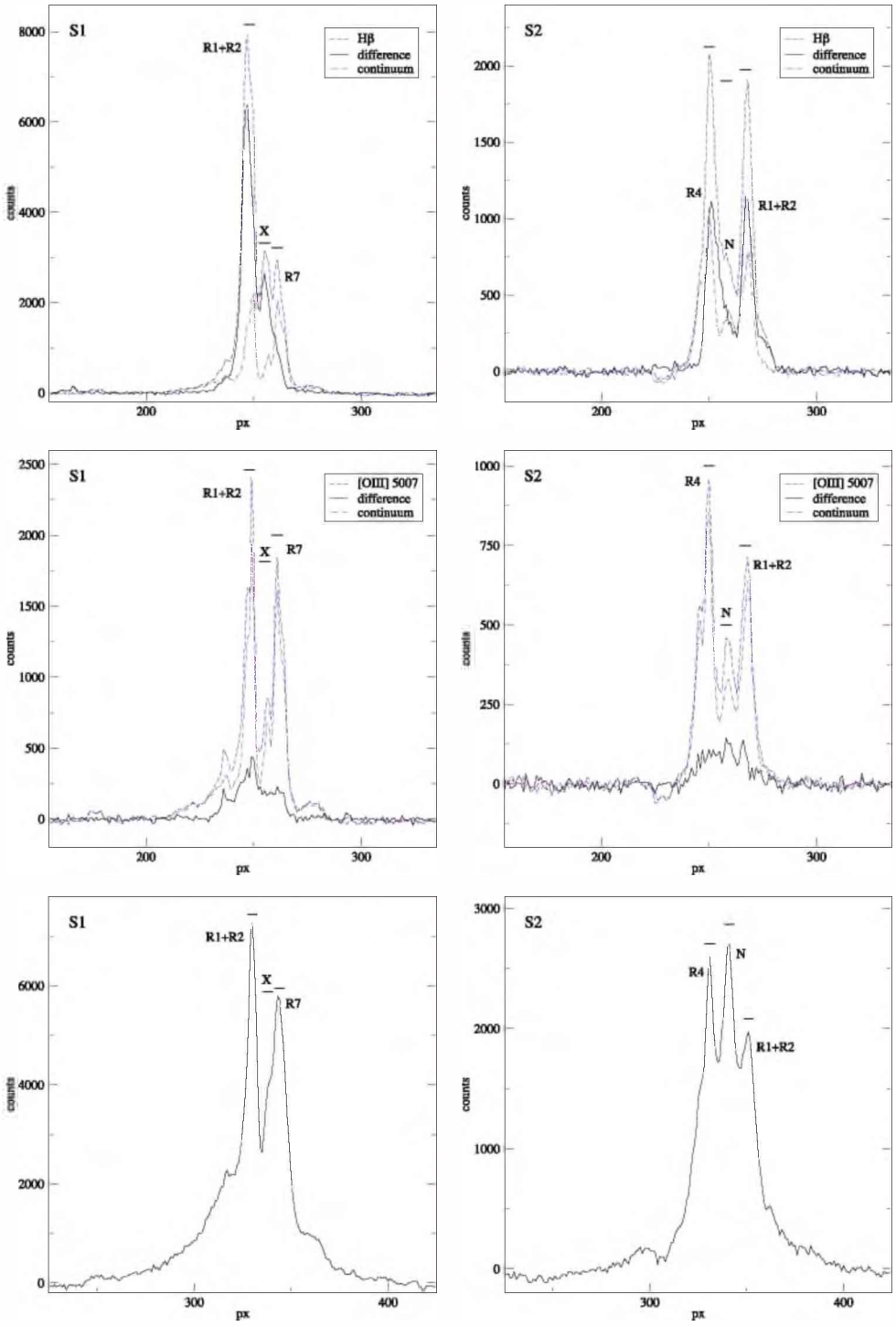

Figure 2. Spatial profiles of Hβ, [O III] λ 5007Å and the far red (upper, middle and lower panels, respectively) for each slit. For the emission lines, the profiles correspond to line+continuum (dashed line), continuum (dash–dotted line) and the difference between them (solid line), representing the pure emission from Hβ and [O III], respectively. For the far-red profiles, the solid lines represent the continuum. Pixel number increases to the north. Horizontal small lines show the location of the CNSFRs and nuclear apertures.

contributor comes from the continuum since the actual emission line is very weak as expected for high-metallicity H II regions (Díaz et al. 2007). Spectra in slit position S1 are placed along the circumnuclear regions located to the north and north-east of the nucleus, and therefore any contribution from the underlying galaxy bulge is difficult to assess. In the case of slit position S2 which crosses the galactic nucleus, this fact can be used to estimate that contribution. For the blue spectra, the light from the underlying bulge is almost negligible amounting to, at most, 5 per cent at the Hβ line. For the red spectra, the bulge contribution is more important. From Gaussian fits to the λ 8620 Å continuum profile, we find that it amounts to about 15 per cent for the lowest surface brightness region, R1+R2. On the other hand, the analysis of the broad NIR *HST*–NICMOS image, shown in Fig. 1, indicates less contrast between the emission

from the regions and the underlying bulge which is very close to the image background emission. Its contribution is about 25 per cent for the weak regions, R2 and R7 along position slit S1.

Figs 3 and 4 show that the spectra of the observed regions and the nucleus, respectively, split into two panels corresponding to the blue and the red spectral ranges. The blue spectra show the Balmer Hβ recombination line and the weak collisionally excited [O III] lines at $\lambda\lambda$ 4959, 5007 Å. The red spectra show the stellar CaT lines in absorption at $\lambda\lambda$ 8498, 8542, 8662 Å. In some cases, as for example R1+R2, these lines are contaminated by the Paschen emission which occurs at wavelengths very close to those of the CaT lines. Other emission features, such as O I λ 8446, [Cl II] λ 8579, Pa 14 and [Fe II] λ 8617, are also present. In this case, a single-Gaussian fit to the emission lines was performed and the lines were subsequently subtracted after checking that the theoretically expected ratio between the Paschen lines was satisfied. The observed red spectra of R1+R2 are plotted in Fig. 3 with a dashed line. The solid lines show the subtracted spectra.

Fig. 5 shows the spectrum of the almost pure emission knot marked in the profiles of NGC 2903, region X. In this case, the blue range of the spectrum presents very intense emission lines, while in the red range we can appreciate a spectrum similar to those shown by the CNSFRs studied by Planesas et al. (1997) suggesting a region with similar characteristics but with low continuum surface brightness.

3.1 Kinematics of stars and ionized gas

A detailed description of the methods and techniques used to derive the values of radial velocities and velocity dispersions as well as sizes, masses and emission line fluxes has been given in Paper I. Therefore, only a brief summary is given below.

3.1.1 Stellar analysis

Stellar radial velocities and velocity dispersions were obtained from the conspicuous CaT absorption lines using the cross-correlation technique, described in detail by Tonry & Davis (1979). This method requires the comparison with a stellar template that represents the stellar population that best reproduces the absorption features. This has been built from a set of 11 late-type giant and supergiant stars with strong CaT absorption lines. We have followed the work by Nelson & Whittle (1995) with the variation introduced by Palacios et al. (1997) of using the individual stellar templates instead of an average. This procedure will allow us to correct for the known possible mismatches between template stars and the region composite spectrum. The implementation of the method in the external package of IRAF XCSAO (Kurtz & Mink 1998) has been used, as explained in Paper I.

To determine the line-of-sight stellar velocity and velocity dispersion along each slit, extractions were made every 2 pixels for slit position S1 and every 3 pixels for slit position S2, with 1 pixel overlap between consecutive extractions in this latter case. In this way, the signal-to-noise ratio (S/N) and the spatial resolution were optimized. The stellar velocity dispersion was estimated at the position of each CNSFR and the nucleus using an aperture of 5 pixels in all cases, which corresponds to 1.0×1.8 arcsec^2. The velocity dispersion (σ) of the stars (σ_*) is taken as the average of the σ values found for each stellar template, and its error is taken as the dispersion of the individual values of σ and the rms of the residuals of the wavelength fit. These values are listed in Column 3 of Table 2 along with their corresponding errors.

The radial velocities have been determined directly from the position of the main peak of the cross-correlation of each galaxy spectrum with each template in the rest frame. The average of these values is the final adopted radial velocity.

3.1.2 Ionized gas analysis

The velocity dispersion of the ionized gas was estimated for each observed CNSFR and for the galaxy nucleus from Gaussian fits to the Hβ and [O III] λ 5007 Å emission lines using 5 pixel apertures, corresponding to 1.0×1.9 arcsec^2. For a single-Gaussian fit, the position and width of a given emission line are taken as the average of the fitted Gaussians to the whole line using three different suitable continua (Jiménez-Benito et al. 2000), and their errors are given by the dispersion of these measurements taking into account the rms of the wavelength calibration.

In all the studied regions, however, the best fit for the Hβ line is obtained with two different components having different radial velocities of up to 35 km s^{-1}. We used the widths of those components as an initial approximation to fit the [O III] lines which, due to their intrinsic weakness, show lower S/N and found them to provide an optimal two-component fit also. The radial velocities found for the narrow (broad) components of both Hβ and [O III] are the same within the errors. An example of the two-Gaussian fit is shown in Fig. 6.

For each CNSFR, the gas velocity dispersions for the Hβ and [O III] λ 5007 Å lines derived using single- and double-line Gaussian fit, and their corresponding errors are listed in Table 2. Columns 4 and 5, labelled 'One component', give the results for the single-Gaussian fit. Columns 6 and 7, and 8 and 9, labelled 'Two components – Narrow' and 'Two components – Broad', respectively, list the results for the two-component fits. The last column of the table, labelled $\Delta v_{\rm nb}$, gives the velocity difference between the narrow and broad components. This is calculated as the average of the Hβ and [O III] fit differences. Taking into account the errors in the two-component fits, the errors in these velocity differences vary from 10 to 15 km s^{-1}.

We have also determined the distribution along each slit position of the radial velocities and the velocity dispersions of the ionized gas using the same procedure as in the case of the stars, that is using spectra extracted every 2 pixels for S1 and every 3 pixels, superposing 1 pixel for consecutive extractions, for S2. These spectra, however, do not have the required S/N to allow an acceptable two-component fit, therefore a single-Gaussian component has been used. The goodness of this procedure is discussed in Section 4.

3.2 Emission line ratios

We have used two different ways to integrate the intensity of a given line: (1) if an adequate fit was attained by a single Gaussian, the emission line intensities were measured using the SPLOT task in IRAF. For the Hβ emission lines, a conspicuous underlying stellar population is inferred from the presence of absorption features that depress the lines (e.g. see discussion in Díaz 1988). Examples of this effect can be appreciated in Fig. 7. We have defined a pseudo-continuum at the base of the line to measure the line intensities and minimize the errors introduced by the underlying population (for details see Hägele et al. 2006). (2) When the optimal fit was obtained by two Gaussians, the individual intensities of the narrow and broad components are estimated from the fitting parameters ($I = 1.0645\,A \times \mathrm{FWHM} = \sqrt{2\pi}\,A\,\sigma$; where I is the Gaussian

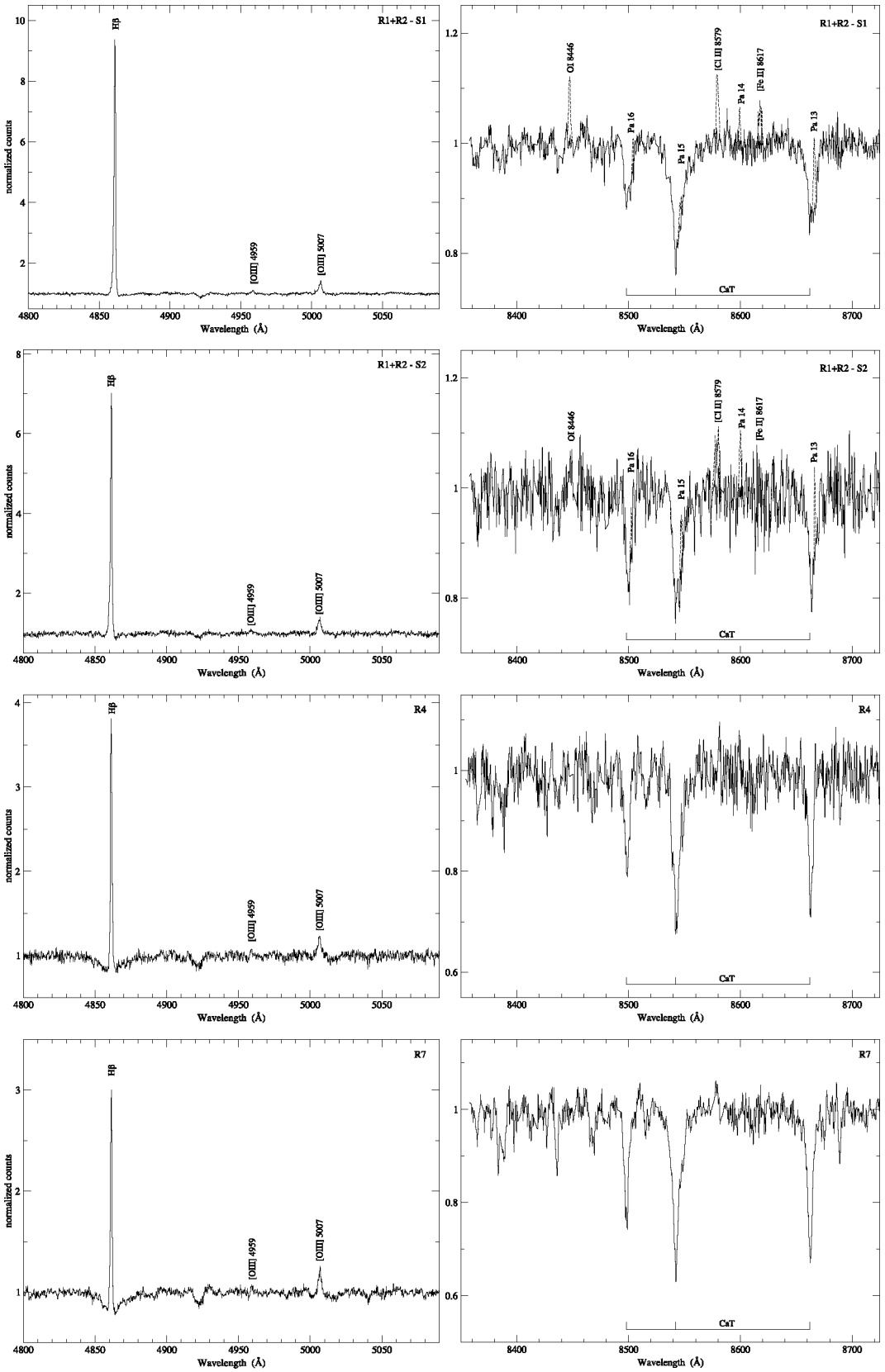

Figure 3. Blue (left-hand panels) and red (right-hand panels) rest-frame normalized spectra of the observed CNSFRs. For R1+R2, the dashed line shows the obtained spectrum; the solid line represents the spectrum after subtracting the emission lines (see the text). Note the absence of conspicuous emission lines in the red spectral range for R4 and R7.

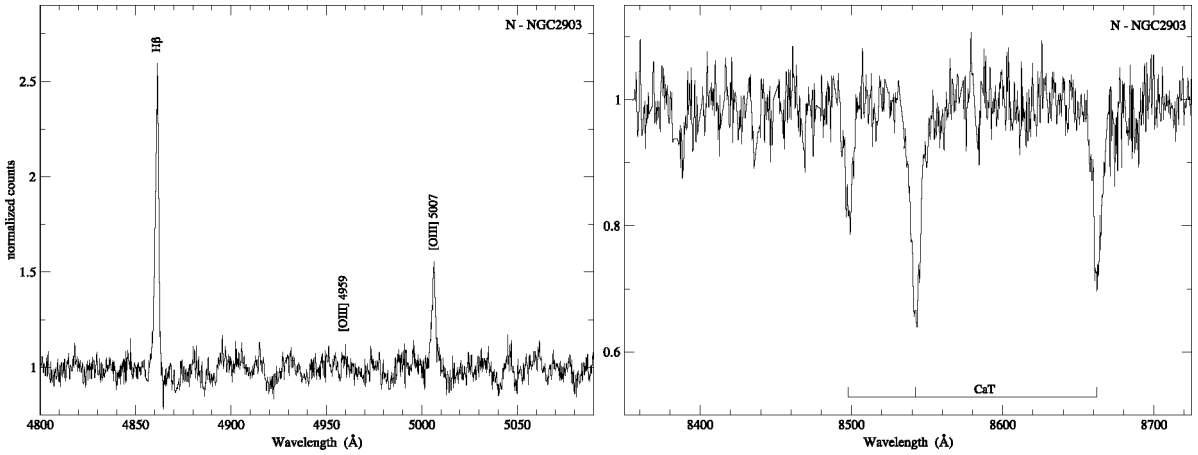

Figure 4. Blue (left-hand panel) and red (right-hand panel) rest-frame normalized spectra of the nucleus.

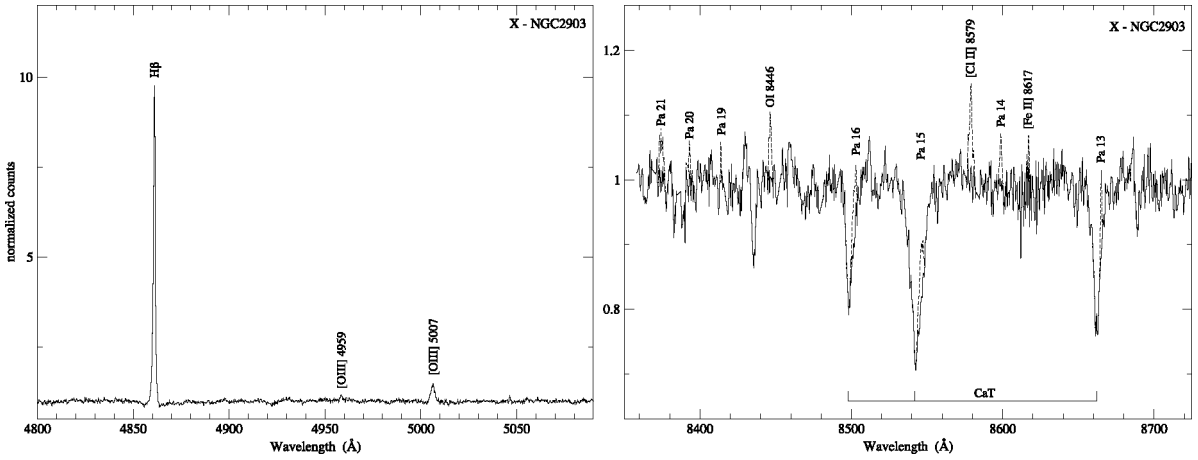

Figure 5. As Fig. 3 for region X. The dashed line shows the obtained spectrum; the solid line represents the spectrum after subtracting the emission lines (see the text).

Table 2. Velocity dispersions.

			One component		Two components				
					Narrow		Broad		
Region	Slit	σ_*	$\sigma_{\rm gas}(H\beta)$	$\sigma_{\rm gas}([O\,III])$	$\sigma_{\rm gas}(H\beta)$	$\sigma_{\rm gas}([O\,III])$	$\sigma_{\rm gas}(H\beta)$	$\sigma_{\rm gas}([O\,III])$	$\Delta v_{\rm nb}$
R1+R2	S1	60±3	34±2	73±8	23±2	26±8	51±3	93±9	30
R1+R2	S2	64±3	35±2	71±9	27±2	27±7	53±4	95±10	35
R4	S2	44±3	32±2	76±10	20±2	35±9	47±4	89±8	−10
R7	S1	37±3	32±4	59±10	29±5	17±5	34±8	67±8	35
N	S2	65±3	59±3	59±7	47±4	27±7	99±13	83±12	20
X	S1	38±3	32±2	66±7	22±2	29±5	54±4	75±8	15

Note. Velocity dispersions in km s^{-1}.

intensity, A is the amplitude of the Gaussian, FWHM is the full width at half-maximum and σ is the dispersion of the Gaussian). A pseudo-continuum for the Hβ emission line was also defined in these cases. The statistical errors associated with the observed emission fluxes have been calculated with the expression $\sigma_1 = \sigma_c N^{1/2}[1 + {\rm EW}/(N\Delta)]^{1/2}$, where σ_1 is the error in the observed line flux, σ_c represents the standard deviation in a box near the measured emission line and stands for the error in the continuum placement, N is the number of pixels used in the measurement of the line intensity, EW is the line equivalent width and $\Delta$is the wavelength dispersion in Å pixel^{-1} (González-Delgado et al. 1994). For the Hβ emission line, we have doubled the derived error, σ_1, in order to take into account the uncertainties introduced by the presence of the underlying stellar population (Hägele et al. 2006).

The logarithmic ratio between the emission line intensities of [O III] λ 5007 Å and Hβ and their corresponding errors are presented in Table 3. We have also listed the logarithmic ratio between the emission line fluxes of [N II] λ 6584 Å and Hα together with their corresponding errors from Díaz et al. (2007) for R1+R2 and R4, and from Planesas et al. (1997) for R7 and the nucleus. For these last two objects, the [N II] and Hα emission are derived from the Hα+[N II] narrow-band images. Planesas and collaborators estimated the relative contribution of the [N II] λλ 6548, 6584 Å lines from the Hα and [N II] λ 6584 Å EW measurements of Stauffer (1982). The

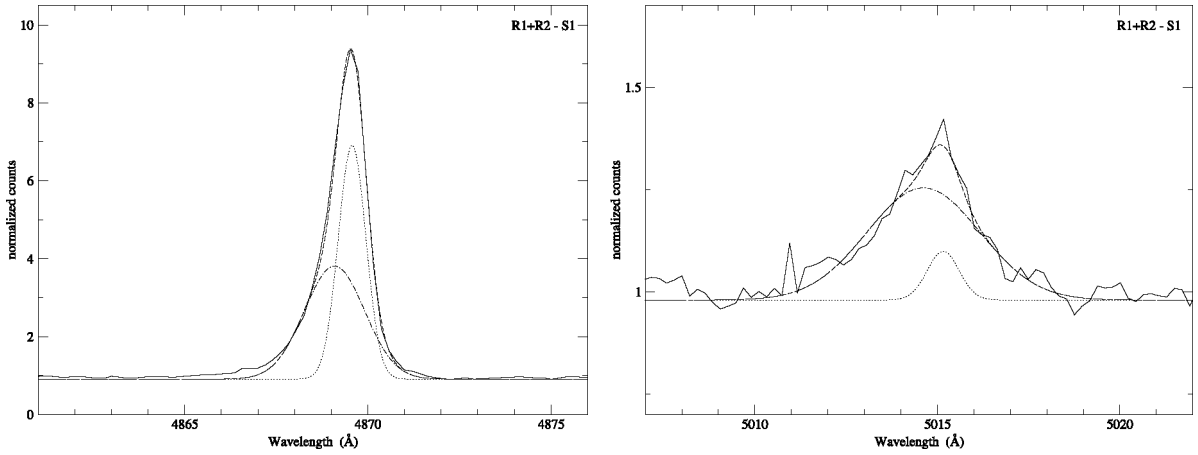

Figure 6. Sections of the normalized spectrum of R1+R2 (solid line). The left-hand panel shows from 4861 to 4876 Å containing Hβ and the right-hand panel shows from 5007 to 5022 Å containing the [O III] λ 5007 Å emission line. For both, we have superposed the fits from the NGAUSSFIT task in IRAF; the dash–dotted line is the broad component, the dotted line is the narrow component and the dashed line is the sum of both.

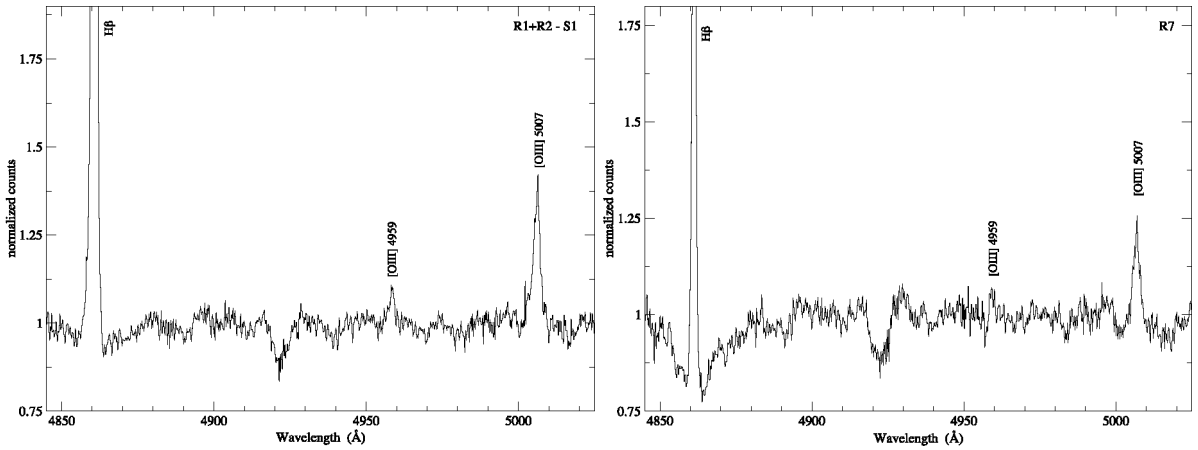

Figure 7. Enlargement of the blue rest-frame normalized spectra of R1+R2 (left-hand panel) and R7 (right-hand panel).

Table 3. Line ratios.

		One component	Two components		
			Narrow	Broad	
Region	Slit	log([O III]5007/Hβ)	log([O III]5007/Hβ)	log([O III]5007/Hβ)	log([N II]6584/Hα)
R1+R2	S1	−1.03±0.05	−1.64±0.09	−0.76±0.10	−0.37 ± 0.01[a]
R1+R2	S2	−0.92±0.07	−1.51±0.11	−0.57±0.14	
R4	S2	−0.78±0.11	−1.01±0.10	−0.71±0.15	−0.38 ± 0.01[a]
R7	S1	−0.78±0.10	−1.79±0.12	−0.40±0.18	−0.66 ± 0.04[b]
N	S2	−0.50±0.07	−0.92±0.10	−0.23±0.18	−0.68 ± 0.04[b]
X	S1	−0.93±0.06	−1.45±0.09	−0.77±0.11	−0.38:[c]

[a]From Díaz et al. (2007).
[b]From Planesas et al. (1997).
[c]Assumed from the values given by Díaz et al. (2007) for the other observed CNSFRs in NGC 2903.

logarithmic ratios for R1+R2 and R4 derived using this procedure are similar (−0.64 ± 0.04 and −0.65 ± 0.04). For the X region, we assumed a value of −0.38 (without error) for this ratio as given by Díaz et al. (2007) for the other CNSFRs of this galaxy.

4 DYNAMICAL MASS DERIVATION

The mass of a virialized stellar system is given by two parameters: its velocity dispersion and its size.

In order to determine the sizes of the stellar clusters within our observed CNSFRs, we have used the retrieved wide *V HST* image which provides a spatial resolution of 0.045 arcsec pixel^{-1}. At the adopted distance for NGC 2903, this resolution corresponds to 1.9 pc pixel^{-1}. Fig. 8 shows enlargements around the different regions studied with intensity contours overlapped.

We find, as expected, that the four CNSFRs studied here are formed by a large number of individual star-forming clusters. Regions R1 and R2 form an interrelated complex with two main structures: R1 and R2 surrounded by, at least, 31 secondary structures.

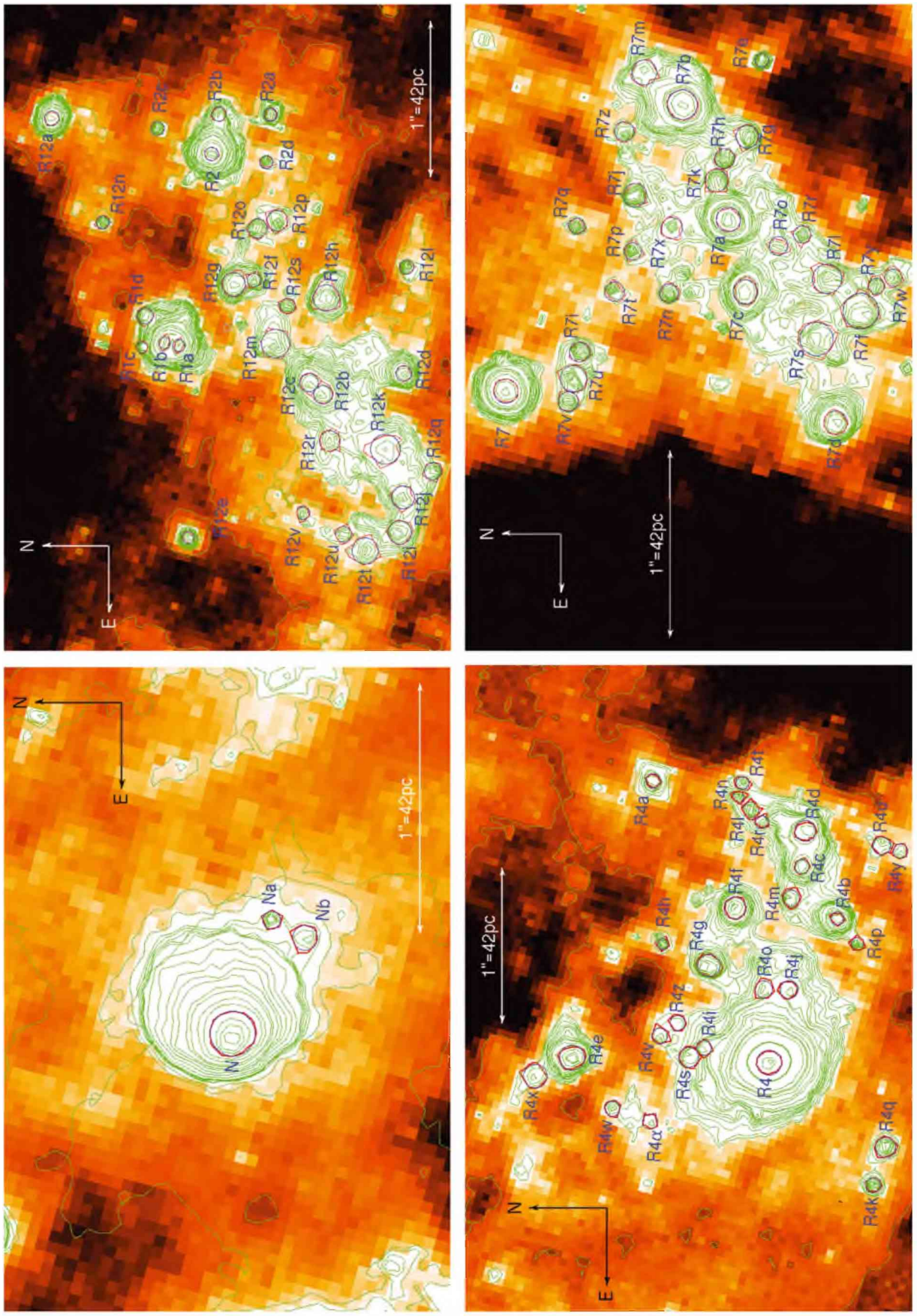

Figure 8. Enlargements of the F606W image around the CNSFRs of our study with the contours overlapped. The circles correspond to the adopted radius for each region. (See the electronic edition of the journal for a colour version of this figure where the adopted radii are in blue and the contours corresponding to the half-light brightness are in red.)

R1 is resolved into two separate clusters, labelled R1a and R1b, and shows other two associated knots, labelled R1c and R1d. R2 is made up of a main cluster, labelled R2, and four secondary ones labelled 'a' to 'd'. The rest of the knots cannot be directly related to any of the two main structures, and have been labelled as R12 followed by a letter from 'a' to 'v'. The same criterion has been applied for regions R4 and R7 for which we find 28 and 27 individual clusters, respectively. On the other hand, the galaxy nucleus seems to be formed by one main structure with two small secondary ones to the south-west, and some very weak knots which are difficult to appreciate in the picture. The secondary structures have been designated by Na and Nb. In all cases, the knots have been found with a detection level of $10\,\sigma$ above the background. All these knots are within the radius of the regions defined by Planesas et al. (1997). We have to remark that our search for knots has not been exhaustive since that is not the aim of this work.

We have fitted circular regions to the intensity contours corresponding to the half-light brightness distribution of each single structure (see Fig. 8), following the procedure given in Meurer et al. (1995), assuming that the regions have a circularly symmetric Gaussian profile. The radii of the single knots vary between 1.5 and 4.0 pc. Table 4 gives, for each identified knot, the position, as given by the astrometric calibration of the *HST* image; the radius of the circular region defined as described above together with its error; and the peak intensity in counts, as measured from the WFPC2 image. The nucleus of NGC 2903 is rather compact, but resolved, with a radius of 3.8 pc. Obviously, the spatial resolution and, at least, the estimates of the smaller radii depend on the distance to each galaxy.

Table 4. Positions, radii and peak intensities derived from the *HST*–F606W image.

Region	Position		R	I	Region	Position		R	I
	$\alpha_{J2000.0}$	$\delta_{J2000.0}$	(pc)	(counts)		$\alpha_{J2000.0}$	$\delta_{J2000.0}$	(pc)	(counts)
R1a	$9^h32^m10^s.06$	$+21°30'06''.86$	1.6±0.1	4083	R4n	$9^h32^m10^s.09$	$+21°29'59''.86$	1.5±0.3	240
R1b	$9^h32^m10^s.06$	$+21°30'06''.95$	1.6±0.2	4015	R4o	$9^h32^m10^s.18$	$+21°29'59''.70$	2.3±0.3	237
R1c	$9^h32^m10^s.07$	$+21°30'07''.10$	1.5±0.1	363	R4p	$9^h32^m10^s.16$	$+21°29'59''.10$	1.6±0.2	236
R1d	$9^h32^m10^s.05$	$+21°30'07''.08$	2.1±0.1	254	R4q	$9^h32^m10^s.25$	$+21°29'58''.92$	2.7±0.3	228
R2	$9^h32^m09^s.98$	$+21°30'06''.65$	1.9±0.1	2892	R4r	$9^h32^m10^s.10$	$+21°29'59''.71$	1.7±0.2	227
R2a	$9^h32^m09^s.96$	$+21°30'06''.28$	1.9±0.1	390	R4s	$9^h32^m10^s.21$	$+21°30'00''.18$	2.7±0.3	216
R2b	$9^h32^m09^s.96$	$+21°30'06''.61$	1.9±0.2	307	R4t	$9^h32^m10^s.08$	$+21°29'59''.83$	1.8±0.2	208
R2c	$9^h32^m09^s.96$	$+21°30'07''.00$	1.9±0.1	209	R4u	$9^h32^m10^s.11$	$+21°29'58''.94$	2.4±0.3	198
R2d	$9^h32^m09^s.98$	$+21°30'06''.30$	1.8±0.2	206	R4v	$9^h32^m10^s.20$	$+21°30'00''.37$	2.1±0.3	196
R12a	$9^h32^m09^s.96$	$+21°30'07''.68$	1.9±0.1	995	R4w	$9^h32^m10^s.23$	$+21°30'00''.67$	2.0±0.2	195
R12b	$9^h32^m10^s.09$	$+21°30'05''.94$	2.5±0.1	580	R4x	$9^h32^m10^s.22$	$+21°30'01''.17$	3.2±0.4	194
R12c	$9^h32^m10^s.08$	$+21°30'06''.03$	2.5±0.1	574	R4y	$9^h32^m10^s.12$	$+21°29'58''.82$	1.9±0.3	187
R12d	$9^h32^m10^s.08$	$+21°30'05''.42$	2.1±0.1	427	R4z	$9^h32^m10^s.19$	$+21°30'00''.25$	2.0±0.3	180
R12e	$9^h32^m10^s.15$	$+21°30'06''.80$	1.6±0.1	381	R4α	$9^h32^m10^s.24$	$+21°30'00''.43$	2.0±0.3	173
R12f	$9^h32^m10^s.03$	$+21°30'06''.38$	1.8±0.1	341	R7	$9^h32^m10^s.38$	$+21°30'10''.93$	2.7±0.1	984
R12g	$9^h32^m10^s.04$	$+21°30'06''.51$	3.2±0.2	293	R7a	$9^h32^m10^s.32$	$+21°30'09''.74$	2.7±0.2	715
R12h	$9^h32^m10^s.04$	$+21°30'05''.91$	3.6±0.4	266	R7b	$9^h32^m10^s.27$	$+21°30'09''.99$	3.4±0.1	579
R12i	$9^h32^m10^s.15$	$+21°30'05''.45$	3.2±0.3	255	R7c	$9^h32^m10^s.34$	$+21°30'09''.65$	2.7±0.3	520
R12j	$9^h32^m10^s.13$	$+21°30'05''.42$	3.2±0.4	238	R7d	$9^h32^m10^s.39$	$+21°30'09''.17$	2.6±0.2	470
R12k	$9^h32^m10^s.11$	$+21°30'05''.54$	4.0±0.5	233	R7e	$9^h32^m10^s.26$	$+21°30'09''.56$	1.5±0.2	283
R12l	$9^h32^m10^s.03$	$+21°30'05''.40$	1.9±0.1	219	R7f	$9^h32^m10^s.35$	$+21°30'09''.03$	4.0±0.5	270
R12m	$9^h32^m10^s.06$	$+21°30'06''.24$	3.8±0.3	212	R7g	$9^h32^m10^s.29$	$+21°30'09''.64$	2.5±0.2	259
R12n	$9^h32^m10^s.01$	$+21°30'07''.35$	1.8±0.1	209	R7h	$9^h32^m10^s.29$	$+21°30'09''.76$	2.2±0.2	252
R12o	$9^h32^m10^s.01$	$+21°30'06''.36$	2.6±0.2	207	R7i	$9^h32^m10^s.37$	$+21°30'10''.54$	2.3±0.1	248
R12p	$9^h32^m10^s.01$	$+21°30'06''.23$	2.8±0.2	204	R7j	$9^h32^m10^s.31$	$+21°30'10''.24$	2.6±0.2	246
R12q	$9^h32^m10^s.12$	$+21°30'05''.23$	2.3±0.2	203	R7k	$9^h32^m10^s.30$	$+21°30'09''.80$	2.6±0.3	234
R12r	$9^h32^m10^s.11$	$+21°30'05''.89$	2.7±0.4	198	R7l	$9^h32^m10^s.34$	$+21°30'09''.21$	3.2±0.5	231
R12s	$9^h32^m10^s.05$	$+21°30'06''.17$	2.1±0.1	193	R7m	$9^h32^m10^s.26$	$+21°30'10''.19$	2.8±0.2	230
R12t	$9^h32^m10^s.16$	$+21°30'05''.67$	3.5±0.4	187	R7n	$9^h32^m10^s.35$	$+21°30'10''.06$	2.1±0.3	227
R12u	$9^h32^m10^s.15$	$+21°30'05''.81$	2.1±0.2	180	R7o	$9^h32^m10^s.33$	$+21°30'09''.47$	2.1±0.2	226
R12v	$9^h32^m10^s.14$	$+21°30'06''.07$	1.7±0.2	179	R7p	$9^h32^m10^s.33$	$+21°30'10''.25$	1.9±0.1	225
R4	$9^h32^m10^s.21$	$+21°29'59''.66$	3.4±0.1	3772	R7q	$9^h32^m10^s.32$	$+21°30'10''.56$	1.7±0.1	222
R4a	$9^h32^m10^s.08$	$+21°30'00''.41$	1.9±0.2	727	R7r	$9^h32^m10^s.32$	$+21°30'09''.35$	1.9±0.2	217
R4b	$9^h32^m10^s.15$	$+21°29'59''.23$	1.7±0.2	711	R7s	$9^h32^m10^s.36$	$+21°30'09''.27$	3.8±0.5	215
R4c	$9^h32^m10^s.12$	$+21°29'59''.45$	1.9±0.1	703	R7t	$9^h32^m10^s.34$	$+21°30'10''.35$	2.1±0.4	212
R4d	$9^h32^m10^s.11$	$+21°29'59''.43$	2.7±0.2	673	R7u	$9^h32^m10^s.38$	$+21°30'10''.57$	2.9±0.4	209
R4e	$9^h32^m10^s.21$	$+21°30'00''.93$	3.4±0.4	476	R7v	$9^h32^m10^s.39$	$+21°30'10''.60$	2.2±0.2	208
R4f	$9^h32^m10^s.14$	$+21°29'59''.88$	2.9±0.1	429	R7w	$9^h32^m10^s.34$	$+21°30'08''.86$	1.9±0.2	208
R4g	$9^h32^m10^s.17$	$+21°30'00''.05$	2.9±0.4	310	R7x	$9^h32^m10^s.32$	$+21°30'10''.04$	2.4±0.2	207
R4h	$9^h32^m10^s.16$	$+21°30'00''.35$	1.5±0.2	279	R7y	$9^h32^m10^s.34$	$+21°30'08''.95$	1.7±0.1	206
R4i	$9^h32^m10^s.21$	$+21°30'00''.09$	2.0±0.3	274	R7z	$9^h32^m10^s.28$	$+21°30'10''.30$	2.2±0.1	204
R4j	$9^h32^m10^s.18$	$+21°29'59''.54$	2.4±0.2	271	N	$9^h32^m10^s.14$	$+21°30'03''.04$	3.8±0.1	870
R4k	$9^h32^m10^s.27$	$+21°29'58''.99$	2.0±0.2	253	Na	$9^h32^m10^s.11$	$+21°30'02''.88$	1.5±0.2	186
R4l	$9^h32^m10^s.10$	$+21°29'59''.78$	2.1±0.3	246	Nb	$9^h32^m10^s.12$	$+21°30'02''.75$	2.1±0.2	181
R4m	$9^h32^m10^s.14$	$+21°29'59''.52$	2.2±0.3	245					

Upper limits to the dynamical masses (M_*) inside the half-light radius (R) for each observed knot have been estimated under the following assumptions: (i) the systems are spherically symmetric; (ii) they are gravitationally bound and (iii) they have isotropic velocity distributions [σ^2 (total) = $3\sigma_*^2$]. The general expression for the virial mass of a cluster is $\eta\,\sigma_*^2\,R/G$, where R is the effective gravitational radius and η is a dimensionless number that takes into account departures from isotropy in the velocity distribution and the spatial mass distribution, binary fraction, mean surface density, etc. (Boily et al. 2005; Fleck et al. 2006). Following Ho & Filippenko (1996a,b), and for consistency with Paper I and Hägele (2008), we obtain the dynamical masses inside the half-light radius using η = 3 and adopting the half-light radius as a reasonable approximation of the effective radius. Other authors (e.g. Spitzer 1987; Smith & Gallagher 2001; Moll et al. 2008) assumed that the η value is about 9.75 thus obtaining the total mass. In the absence of any knowledge about the tidal radius of the clusters, we adopted this conservative approach. On the derived masses, the different adopted η values act as multiplicative factors.

It must be noted that we have measurements for the size of each knot, but we do not have direct access to the stellar velocity dispersion of each individual cluster, since our spectroscopic measurements encompass a wider area (1.0 × 1.9 arcsec^2, which corresponds approximately to 42 × 76 pc^2 at the adopted distance of NGC 2903) that includes the whole CNSFRs to which each group of knots belong.

The estimated dynamical masses for each knot and their corresponding errors are listed in Table 5. For the regions that have been observed in more than one slit position, we list the derived values using the two separate stellar velocity dispersions. The dynamical masses in the rows labelled 'sum' have been found by adding the individual masses in a given CNSFR: R12, R4 and R7, as well as

Table 5. Dynamical masses.

Region	Slit	M_*	Error (per cent)	Region	Slit	M_*	Error (per cent)	Region	Slit	M_*	Error (per cent)
R1a	S1	40±5	12	R12b	S2	71±6	9	R4s	S2	36±6	17
R1b	S1	39±6	17	R12c	S2	71±6	9	R4t	S2	24±4	17
R1c	S1	37±5	13	R12d	S2	59±6	9	R4u	S2	33±6	18
R1d	S1	52±6	12	R12e	S2	45±5	10	R4v	S2	29±5	19
R2	S1	46±6	12	R12f	S2	51±5	10	R4w	S2	27±4	16
R2a	S1	47±6	12	R12g	S2	89±9	10	R4x	S2	43±8	18
R2b	S1	47±7	15	R12h	S2	101±13	13	R4y	S2	26±5	20
R2c	S1	46±6	12	R12i	S2	89±11	12	R4z	S2	27±5	20
R2d	S1	44±7	16	R12j	S2	91±13	14	R4α	S2	27±5	20
R12a	S1	47±6	12	R12k	S2	113±16	14	R4sum	S2	853±28	3
R12b	S1	63±7	11	R12l	S2	53±5	10	R7	S1	26±5	18
R12c	S1	63±7	11	R12m	S2	107±12	11	R7a	S1	26±5	19
R12d	S1	52±6	12	R12n	S2	50±5	10	R7b	S1	32±6	17
R12e	S1	40±5	12	R12o	S2	72±8	11	R7c	S1	26±5	20
R12f	S1	45±5	12	R12p	S2	79±8	10	R7d	S1	25±5	19
R12g	S1	79±10	12	R12q	S2	65±7	11	R7e	S1	14±3	22
R12h	S1	89±14	15	R12r	S2	77±12	15	R7f	S1	38±8	21
R12i	S1	79±11	14	R12s	S2	59±6	9	R7g	S1	24±5	19
R12j	S1	81±13	16	R12t	S2	100±13	13	R7h	S1	21±4	19
R12k	S1	100±16	16	R12u	S2	59±7	12	R7i	S1	22±4	18
R12l	S1	47±6	12	R12v	S2	47±6	13	R7j	S1	25±5	19
R12m	S1	94±13	13	R12sum	S2	2054±45	2	R7k	S1	25±5	21
R12n	S1	44±5	12	R12 (adopted)		1935±66	3	R7l	S1	31±7	23
R12o	S1	64±8	13	R4	S2	46±6	13	R7m	S1	27±5	19
R12p	S1	70±9	13	R4a	S2	26±4	16	R7n	S1	20±5	22
R12q	S1	58±8	14	R4b	S2	23±4	17	R7o	S1	20±4	20
R12r	S1	68±12	18	R4c	S2	26±4	14	R7p	S1	19±3	18
R12s	S1	52±6	12	R4d	S2	37±5	15	R7q	S1	17±3	18
R12t	S1	88±14	16	R4e	S2	46±8	17	R7r	S1	18±4	20
R12u	S1	52±7	14	R4f	S2	40±5	13	R7s	S1	36±8	22
R12v	S1	42±7	16	R4g	S2	40±7	19	R7t	S1	21±5	25
R12sum	S1	1816±48	3	R4h	S2	20±4	19	R7u	S1	28±6	22
R1a	S2	45±5	10	R4i	S2	27±5	20	R7v	S1	21±4	19
R1b	S2	44±6	14	R4j	S2	32±5	15	R7w	S1	19±4	20
R1c	S2	41±4	10	R4k	S2	27±4	16	R7x	S1	23±4	19
R1d	S2	59±6	9	R4l	S2	29±5	19	R7y	S1	17±3	18
R2	S2	52±5	10	R4m	S2	30±6	18	R7z	S1	21±4	18
R2a	S2	53±5	10	R4n	S2	20±5	24	R7sum	S1	642±26	4
R2b	S2	53±7	13	R4o	S2	31±6	18	N	S2	112±10	9
R2c	S2	52±5	10	R4p	S2	22±4	18	Na	S2	43±7	16
R2d	S2	50±6	13	R4q	S2	36±6	17	Nb	S2	62±8	13
R12a	S2	53±5	10	R4r	S2	23±4	17	Nsum	S2	217±15	7

Note. Masses in 10^5 $M_\odot$.

Table 6. Physical parameters.

Region	$L_{obs}(H\alpha)^a$	$E(B-V)^b$	$c(H\alpha)$	$L(H\alpha)$	$Q(H_0)$	EW(Hβ)	M_{ion}	N_e	M_{HII}	M_{ion}/M_* (per cent)
R1+R2	20.3	0.53	0.52	66.3	48.7	12.1	18.9	280[c]	0.79	1.0
R4	8.9	0.66	0.64	38.9	28.6	4.8	24.6	270[c]	0.48	2.9
R7	6.4	0.71	0.69	31.3	23.0	3.9	23.6	350[b]	0.30	3.7
N[d]	2.8	—	—	2.8	2.0	3.8	2.1	—	0.03	1.0

Note. Luminosities in 10^{38} erg s^{-1}, masses in 10^5 M$_\odot$, ionizing photons in 10^{50} photon s^{-1} and densities in cm^{-3}.
[a]From Planesas et al. (1997) corrected for the different adopted distance.
[b]From Pérez-Olea (1996).
[c]From Díaz et al. (2007).
[d]We assume a value of 0.0 and 300 for $E(B-V)$ and N_e, respectively.

the galaxy nucleus, N. We have taken the average of the R12sum estimated from slit positions S1 and S2 as the 'adopted' dynamical mass for R12. The fractional errors of the dynamical masses of the individual knots and of the CNSFRs are listed in Column 4.

5 IONIZING STAR CLUSTER PROPERTIES

For each of the CNSFR: R12, R4 and R7, the total number of ionizing photons was derived from the total observed Hα luminosities given by Planesas et al. (1997), correcting for the different assumed distance. We also corrected for internal extinction using the colour excess $[E(B-V)]$ estimated by Pérez-Olea (1996) from optical spectroscopy and assuming the galactic extinction law of Miller & Mathews (1972) with $R_v = 3.2$. Planesas et al. (1997) estimated a diameter of 2.0 arcsec for regions R1, R2, R7 and the nucleus and 2.4 arcsec for region R4. In the case of R1+R2, we added their Hα luminosities. No values are found in the literature for the Hα luminosity of region X. Our derived values of $Q(H_0)$ constitute lower limits since we have not taken into account the fraction of photons that may have been absorbed by dust or may have escaped the region.

Once the number of Lyman continuum photons has been calculated, the masses of the ionizing star clusters, M_{ion}, have been derived using the solar metallicity single burst models by García-Vargas, Bressan & Díaz (1995) which provide the number of ionizing photons per unit mass, $[Q(H_0)/M_{ion}]$. A Salpeter initial mass function (Salpeter 1955; IMF) has been assumed with lower and upper mass limits of 0.8 and 120 M$_\odot$. In order to take into account the evolution of the H II region, we have made use of the fact that a relation exists between the degree of evolution of the cluster, as represented by the EW of the Hβ emission line, and the number of Lyman continuum photons per unit solar mass (e.g. Díaz et al. 2000b). We have measured the EW(Hβ) from our spectra (see Table 6) following the same procedure as in Hägele et al. (2006, 2008) that is defining a pseudo-continuum to take into account the absorption from the underlying stellar population. This procedure in fact may underestimate the value of the EW, since it includes the contribution to the continuum by the older stellar population (see discussions in Díaz et al. 2007 and Dors et al. 2008). The derived masses for the ionizing population of the observed CNSFRs are given in Column 8 of Table 6 and are between 1 and 4 per cent of the dynamical mass (see Column 11 of the table).

The amount of ionized gas (M_{HII}) associated with each star-forming region complex can also be derived from the Hα luminosities using the electron density (N_e) dependency relation given by Macchetto et al. (1990) for an electron temperature of 10^4 K. The electron density for each region (obtained from the [S II] $\lambda\lambda$ 6717/6731 Å line ratio) has been taken from Díaz et al. (2007) for R1+R2 and R4 and Pérez-Olea (1996) for R7 (see Table 6). A value of N_e equal to 300 cm^{-3}, typical of nuclear H II regions, has been assumed for the nucleus.

6 DISCUSSION

6.1 Star and gas kinematics

The relations between the velocity dispersions of gas, as measured from the Hβ (upper panel) and the [O III] (lower panel) emission lines, and stars, as measured from the IR CaT, are shown in Fig. 9. In both panels, the straight line shows the one-to-one relation. In the upper panel, red[3] circles show the gas velocity dispersion measured from the Hβ emission line using a single-Gaussian fit. Orange squares and magenta downward triangles show the values measured from the broad and narrow components, respectively, using two-component Gaussian fits. The deviant point, marked with arrows, corresponds to the galaxy nucleus, whose spectra have a low S/N and for which the fits do not provide accurate results for the broad component. In the lower panel, red upward triangles, orange diamonds and magenta left triangles correspond to the values obtained by a single-Gaussian fit, and to the broad and narrow components of the two Gaussian fits, respectively.

In general, the Hβ velocity dispersions of the CNSFRs of NGC 2903 derived by a single-Gaussian fit are lower than the stellar ones by about 25 km s^{-1}, except for regions R7 and X, for which these values are very similar. These two regions also have the lowest velocity dispersions, and in the first of them the values derived using the two different fitting procedures are very similar. On the other hand, a much better agreement between the velocity dispersions of stars and the broad component of Hβ for the CNSFRs is found. The narrow component shows velocity dispersions even lower than those obtained by single-Gaussian fits, and similar to each other in all cases, with an average value equal to 24.5 ± 2.2 km s^{-1}, with the error given by the dispersion of the individual values. This average is represented as a magenta horizontal line in the upper panel of Fig. 9, with its error as magenta dashed lines.

The [O III] lines, however, show a behaviour different from the Hβ lines. In this case, for all the CNSFRs, the gas velocity dispersions derived by a single-Gaussian fit are higher by different amounts, between 7 and 32 km s^{-1}. When a two-component fitting procedure is used, the narrow component shows the same average value found for the Hβ line, although with a larger dispersion ($\sigma_g = 26.2 \pm$

[3] In all figures, colours can be seen in the electronic version of the paper.

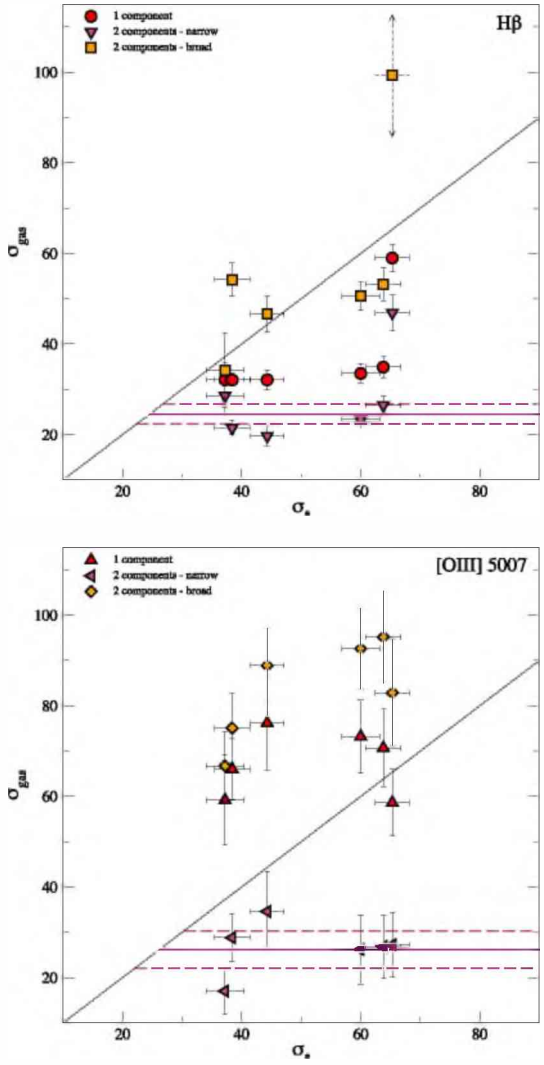

Figure 9. Upper panel: relation between velocity dispersions of the gas (derived from Hβ) and stars (CaT) for the CNSFRs and the nucleus of NGC 2903. Symbols are as follows: single-Gaussian fit, (red) circles; two Gaussian fit, broad component, (orange) squares; narrow component, (magenta) downward triangles. Lower panel: as the upper panel for the [O III] line. (Red) upward triangles correspond to the estimates using a single-Gaussian fit, (orange) diamonds represent the broad components of the two Gaussian fit and (magenta) left triangles, the narrow components. The (magenta) line represents the average velocity dispersion of the narrow component of the gas (Hβ upper and [O III] lower panel) for the CNSFRs, and the (magenta) dashed lines represent their estimated errors. (See the electronic edition of the journal for a colour version of this figure.)

4.2 km s^{-1}), while the broad component shows values even larger than those derived from single-Gaussian fits. It is therefore apparent that if there are two kinematically different components in the gas, the narrow one seems to dominate the Hβ line while the broad one seems to dominate the [O III] ones. In fact, the ratio between the fluxes in the narrow and broad components is between 0.65 and 0.95 for the Hβ line (except for the weakest knot R7, for which it is about 1.46) and decreases to between 0.06 and 0.24 for the [O III] line.

These results are similar to those found for the previously analysed spiral galaxy NGC 3351 (see Paper I). The single-Gaussian fit yields velocity dispersions which are lower than measured for the stars in the case of Hβ and higher in the case of [O III] by about 20 km s^{-1}.

When two width Gaussian fits are used, the narrow components show a relatively constant value. The average value of this velocity for the CNSFRs analysed in both galaxies, NGC 3351 and NGC 2903, amounts to 23.2 $\pm$ 1.7 and 25.1 $\pm$ 2.0 km s^{-1} for the Hβ and the [O III] lines, respectively. Also, for the CNSFRs in the two galaxies, velocity dispersions associated with the broad component of Hβ are in very good agreement with the stellar ones, except for one deviant region in NGC 3351 (R5). For the [O III] emission, the broad component shows velocities larger than the stellar ones by up to about 30 km s^{-1}.

If the narrow component is identified with ionized gas in a rotating disc, therefore supported by rotation, then the broad component could, in principle, correspond to the gas response to the gravitational potential of the stellar cluster, supported by dynamical pressure, explaining the coincidence with the stellar velocity dispersion in the case of the Hβ line (see Pizzella et al. 2004 and references therein). The velocity excess shown by the broad component of [O III] could be identified with peculiar velocities in the high-ionization gas related to massive star winds or even supernova remnants.

While two velocity components are clearly identified in the Hβ line, the weakness of the [O III] lines renders this identification more uncertain. To test the possibility of finding a spurious result due to the low S/N in the weak [O III] emission lines, we generated a synthetic spectrum with the measured characteristics of radial velocity and FWHM adding an artificial noise with a rms twice the observed one. We then measured the synthetic spectra using the same technique used for the real data that is a double-Gaussian fitting with the same initial parameters. In all cases, we obtained the same result within the observational errors.

Our interpretation of the emission line structures, in this study and in Paper I, parallels that of the studies of Westmoquette and collaborators (see e.g. Westmoquette et al. 2007a,b). They observed a narrow (~35–100 km s^{-1}) and a broad (~100–400 km s^{-1}) component to the Hα line across all their four fields in the dwarf galaxy NGC 1569. They conclude that the most likely explanation of the narrow component is that it represents the general disturbed optically emitting ionized interstellar medium (ISM), arising through a convolution of the stirring effects of the starburst and gravitational virial motions. They also conclude that the broad component results from the highly turbulent velocity field associated with the interaction of the hot phase of the ISM (material that is photo-evaporated or thermally evaporated through the action of the strong ambient radiation field, or mechanically ablated by the impact of fast-flowing cluster winds) with cooler gas knots, setting up turbulent mixing layers (e.g. Begelman & Fabian 1990; Slavin, Shull & Begelman 1993). However, our broad component velocity dispersion values derived from the Hβ emission lines resemble their narrow component values more, since in all the CNSFRs the former are significantly lower than 100 km s^{-1} and show similar values to the stellar velocity dispersions. The [O III] emission line, on the other hand, shows a behaviour akin to that described by Westmoquette and collaborators.

There are other studies that identified an underlying broad component to the recombination emission lines, such as Díaz et al. (1987) and Terlevich et al. (1996) in the M33 giant H II region NGC 604; Chu & Kennicutt (1994) and Melnick, Tenorio-Tagle & Terlevich (1999) in the central region of 30 Doradus; Mendez & Esteban (1997) in four Wolf–Rayet galaxies and Homeier & Gallagher (1999) in the starburst galaxy NGC 7673. More recently,

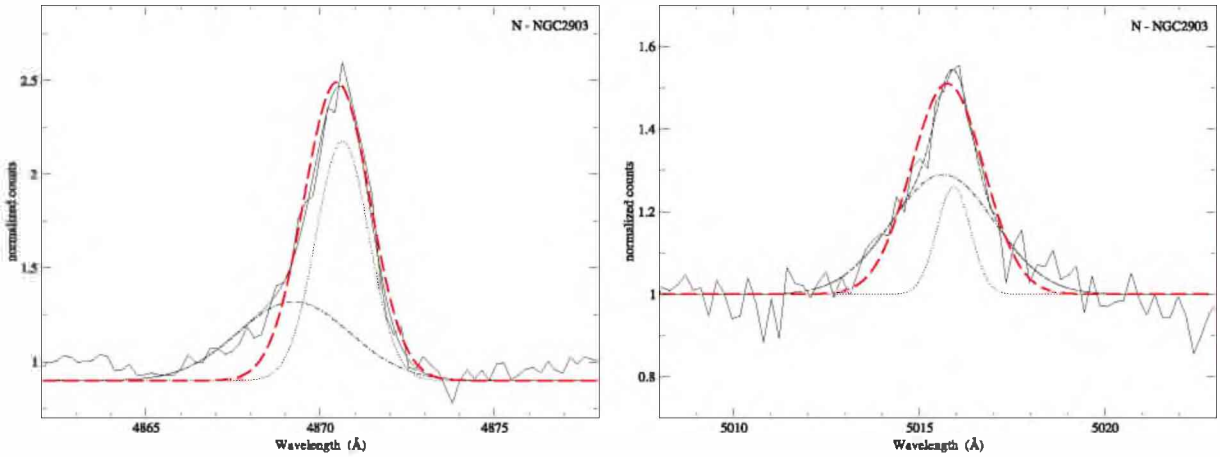

Figure 10. Single- and two-component Gaussian fits for the Hβ (left-hand panel) and [O III] λ 5007 Å (right-hand panel) emission lines in the nucleus of NGC 2903. Thick dashed (red) line and two-component fits as resulting from the IRAF task NGAUSSFIT are superposed. For the two-component fit, the dash–dotted line corresponds to the broad component, the dotted line to the narrow component and the dashed line to the sum of both.

Westmoquette et al. (2007c, 2009) found a broad feature in the Hα emission lines in the starburst core of M82; Östlin, Cumming & Bergvall (2007) in the blue compact galaxy ESO 338-IG04; Sidoli, Smith & Crowther (2006) and Firpo et al. (in preparation) in giant extragalactic H II regions, and Hägele (2008) and Hägele et al. (2009) in CNSFRs of early-type spiral galaxies. The first two and the last four studies also found this broad component in the forbidden emission lines.

Single-Gaussian fits yield the same velocity dispersion in the nucleus for both emission lines, Hβ and [O III] 5007 Å, and close to the stellar value. If a two-component fit is used, the low S/N in the Hβ line, combined with the underlying absorption, yields very uncertain values for the broad component and a value for the narrow component which is closer to the stellar one than in the case of the CNSFRs. The results for the [O III] 5007 Å line are similar to those found for the CNSFRs. Fig. 10 shows the single- and two-component Gaussian fitting for the Hβ and [O III] 5007 Å lines. The *H*β line shows a blue asymmetry which might correspond to a low-intensity broad component. This component is barely detectable (if at all present) in the [O III] 5007 Å line.

If this decomposition of the emission lines is correct, the profiles of the nuclear lines show a behaviour similar to that described by Westmoquette and collaborators, with the velocity dispersion value of the broad component of H$\beta \gtrsim 100\,\mathrm{km\,s^{-1}}$. Using *ROSAT* data, Tschöke, Hensler & Junkes (2003) found a very soft X-ray emission feature that extends to 2 arcmin (~5 kpc) from the nucleus to the west. They concluded that the existence of a galactic wind and its interaction with the surrounding intergalactic medium are the most plausible source for this soft emission. The Hβ broad feature thus could be consistent with the presence of a nuclear region galactic wind, which could arise from gas that is mixing into a high sound speed, hot gas phase, whose presence dominates X-ray images, as in NGC 1569 (Westmoquette et al. 2007a,b).

The presence of two different gaseous components in our analysed CNSFR could have an important effect on the classification of the activity in the central regions of galaxies through diagnostic diagrams and the magnitude of this effect would increase with decreasing spatial resolution. In fact, the [O III]/Hβ ratio is much smaller for the narrow component than for the broad one, and single-Gaussian fittings provide intermediate values (see Table 2). This seems to point to a lower excitation for the lower velocity kinematical component. The effect is rather dramatic even for the nucleus of NGC 2903 for which the logarithmic [O III]/Hβ ratio for the low- and high-velocity components vary from −0.91 to −0.22. Unfortunately, we do not have high-resolution data in the [N II]–Hα wavelength range, and hence we cannot investigate the complete effect in the excitation plot (see Paper I).

The radial velocities along the slit for each angular position of NGC 2903 as derived from the ionized gas emission lines, Hβ and [O III] 5007 Å, and the stellar CaT absorptions are shown in the upper and lower panels of Fig. 11, respectively. The rotation curves seem to have the turnover points at the same positions as the star-forming ring, specially for the S2 slit position across the nucleus, as found in other galaxies (see Telesco & Decher 1988; Díaz et al. 1999, and references therein). For the systemic velocity of NGC 2903, the derived values are consistent with those previously obtained by Planesas et al. (1997) and Haynes et al. (1998), and with the velocity distribution expected for this type of galaxies (Binney & Tremaine 1987).

The radial velocities derived from both the stellar CaT and the [O III] 5007 Å emission line are in good agreement. The Hβ line velocities, however, differ from the stellar ones, more appreciably in the north-west region, in amounts similar to the differences shown by the radial velocities corresponding to the two Gaussian components (Δv_{nb}; see Table 2). This is compatible with the assumption of the existence of two kinematically different components, the broad one dominating the single fit in [O III] and the narrow one being the dominant one in the case of Hβ.

Fig. 12 shows the run of velocity dispersions along the slit versus pixel number for slit positions S1 and S2 of NGC 2903, respectively. These velocity dispersions have been derived from the gas emission lines, Hβ and [O III], and the stellar absorption ones using 2 and 3 pixel apertures for S1 and S2, respectively. We have marked the location of the studied CNSFR and the galaxy nucleus. We have also plotted the stellar velocity dispersion derived for each region and the nucleus using the 5 pixel apertures. The values derived with wider apertures are approximately the average of the velocity dispersions estimated using the narrower apertures. Then, the increase of the apparent velocity dispersions of the regions lying on relatively steep parts of the rotation curve by spatial 'beam smearing' of the rotational velocity gradient due to the finite angular resolution of the spectra is no so critical for the studied CNSFRs. This is due to the fact that turnover points of the rotation curves and the star-forming ring seem to be located at the same positions, as was pointed out

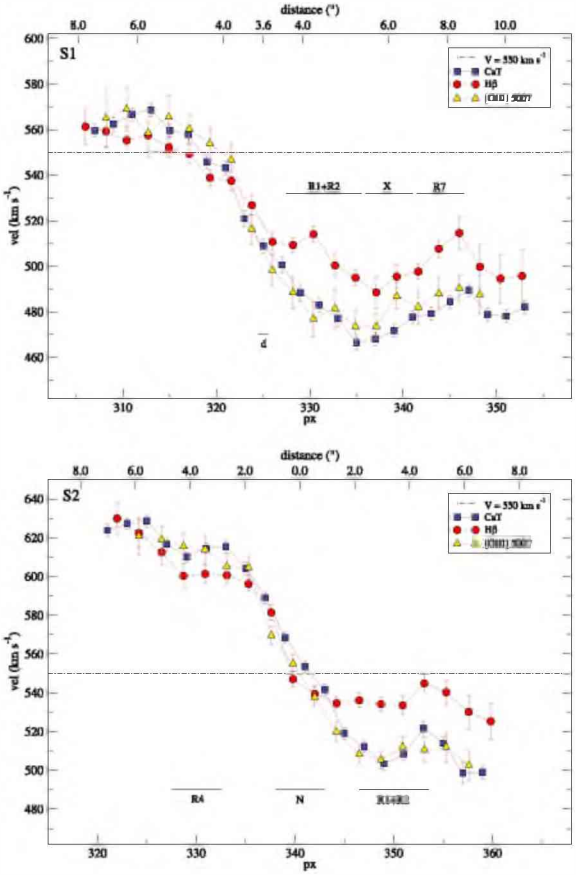

Figure 11. Radial velocities along the slit versus pixel number for each slit position of NGC 2903 (upper panel: S1; lower panel: S2) as derived from the gas emission lines (red circles: Hβ; upward triangles: [O III]) and the stellar absorption ones (blue squares). The individual CNSFRs and the nucleus, 'N', or the closest position to it, 'd', are marked in the plots. The dash–dotted line is the systemic velocity of NGC 2903 derived by Planesas et al. (1997). The distance in arcsec from the nucleus is displayed in the upper x-axis of each panel. (See the electronic edition of the journal for a colour version of this figure.)

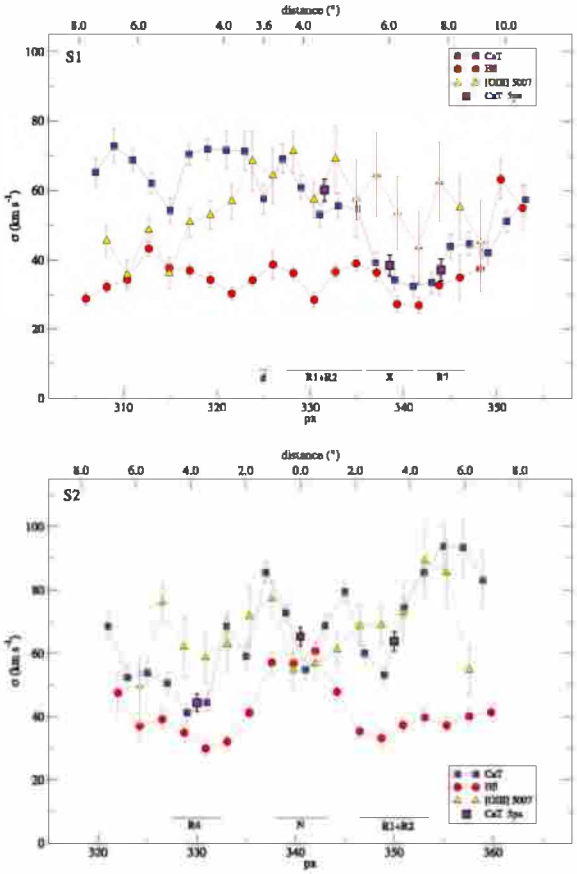

Figure 12. Velocity dispersions along the slit versus pixel number for each slit position of NGC 2903 (upper panel: S1; lower panel: S2) as derived from the gas emission lines (small red circles: Hβ; small yellow triangles: [O III]) and the stellar absorption ones (small blue squares). The stellar velocity dispersions derived for each region and the nucleus using the 5 pixel aperture are also plotted with violet squares. The individual CNSFRs and the nucleus, 'N', or the closest position to it, 'd', are marked in the plots. The distance in arcsec from the nucleus is displayed in the upper x-axis of each panel. (See the electronic edition of the journal for a colour version of this figure.)

above. The behaviour of the velocity dispersion along slit position S1 (upper panel) is very complex. The Hβ line shows a relatively constant value of the velocity dispersion. To the SW of the R1+R2 star-forming complex, there is a clear systematic difference between the velocities measured from the HI recombination line and the stellar absorption lines. This systematic difference is significative lower in the region where active star formation is taking place. Along slit position S2, crossing the galaxy nucleus, we detect relative minima in the stellar and gas velocity dispersions at the positions of CNSFR R4 and R1+R2. The stellar velocity dispersions also show a relative minimum at the location of the nucleus although in this case it is accompanied by a rise in the velocity dispersion measured from the Hβ line.

6.2 Star cluster masses

Unlike the case of the CNSFRs in NGC 3351 studied in Paper I for which we found that two of the observed regions, R4 and R5, seem to possess just one knot showing up in the continuum image and coincident with the Hα emission, the four CNSFRs observed in NGC 2903: R1+R2, R4 and R7 show a complex structure at the *HST* resolution (Fig. 8), with a good number of subclusters with linear diameters between 3 and 8 pc. For these individual clusters, the derived upper limits to the masses are in the range between 1.4×10^6 and 1.13×10^7 $M_\odot$ (see Table 5), with fractional errors between about 9 and 25 per cent. The upper limits to the dynamical masses estimated for the whole CNSFRs ('sum') are between 6.4×10^7 and 1.9×10^8 $M_\odot$, with fractional errors between about 3 and 4 per cent. The upper limit to the dynamical mass derived for the nuclear region inside the inner 3.8 pc is 1.1×10^7 $M_\odot$, with a fractional error of about 9 per cent.

The masses of the ionizing stellar clusters of the circumnuclear complexes have been derived from their Hα luminosities under the assumption that the regions are ionization bound and without taking into account any photon absorption by dust. A range of masses between 1.9 and 2.5×10^6 $M_\odot$ for the star-forming regions, and 2.1×10^5 $M_\odot$ for the nucleus are found (see Table 6). In Column 11 of Table 6, we show a comparison (in percentage) between the ionizing stellar masses of the circumnuclear regions and their dynamical masses. These values are approximately between 1 and 4 per cent for the CNSFRs, and 1 per cent for the nucleus of NGC 2903.

Finally, the masses of the ionized gas, also derived from their Hα luminosities, range between 3×10^4 and 8×10^5 $M_\odot$ for the CNSFRs, and 3×10^3 $M_\odot$ for the nucleus (see Table 6). They make

up a very small fraction of the total mass of the regions. Both the masses of the ionizing stellar clusters and those of the ionized gas are comparable to those derived by González-Delgado et al. (1995) for the circumnuclear region A in NGC 7714. It should be taken into account that the latter have been derived from the Hα luminosity of the CNSFRs assuming a single kinematical component for the emission line. If we consider only the broad component whose kinematics follow that of the stars in the regions, all derived quantities would be smaller by a factor of 2.

The circumnuclear star formation in NGC 2903 has been studied by Alonso-Herrero et al. (2001) using high-resolution NIR photometry in the *H* band and ground-based IR spectroscopy. Although, in general, the spatial distribution of the stellar clusters detected in the IR does not coincide with the maxima of the Hα emission, some CNSFRs show up prominently in both spectral ranges. This is the case for our regions R4, R7 and R1+R2 which can be identified with regions H8, H4 and H1+H2, respectively, in Alonso-Herrero et al. (2001). These authors have estimated the masses of the young clusters present in the central region of NGC 2903 from the NIR colours using stellar population synthesis models corresponding to single bursts of star formation with Gaussian FWHM values of 1, 5 and 100 Myr and a Salpeter IMF with lower and upper mass cut-offs of 1 and 80 $M_\odot$. Values between 2.1×10^8 and 3.6×10^8 $M_\odot$ are obtained for the central ~625 pc region without including the young stellar population responsible for the bright H II region emission. This is consistent with our upper limit to the mass corresponding to the sum of the dynamical mass found for the CNSFR and the nuclear clusters (3.6×10^8 $M_\odot$).

The values of dynamical masses of the individual clusters derived by us for the CNSFRs of both NGC 2903 and NGC 3351 (see Paper I) are larger than those estimated for the individual clusters in the nuclear ring of NGC 4314 from broad-band *U*, *B*, *V*, *I* and Hα photometry with *HST* (Benedict et al. 2002) by more than an order of magnitude. No comparable data exist for the CNSFRs studied here to allow the estimate of photometric M/L ratios. However, the fact that the Hβ luminosities of the NGC 4314 clusters are lower than those of NGC 2903 by a factor of about 40 gives some support to our larger computed dynamical masses. These masses are, on average, of the order of the largest kinematically derived mass for super star clusters (SSCs) in M82 (McCrady & Graham 2007) from NIR spectroscopy (40×10^5 $M_\odot$) but also larger (by factors between 4.2 and 34) than the mass derived for the SSC A in NGC 1569 by Ho & Filippenko (1996a) from stellar velocity dispersion measurements using red (~6000 Å) spectra ($3.3 \pm 0.5 \times 10^5$ $M_\odot$).

It should be recalled that we have estimated the dynamical masses through the virial theorem under the assumption that the systems are spherically symmetric, gravitationally bound and have isotropic velocity distribution. We have used the stellar velocity dispersions derived from the CaT absorptions features and the cluster sizes measured from the high-spatial-resolution WFPC2–PC1 *HST* image.

Therefore, while the average radius of an individual cluster is of the order of 2.8 pc, the stellar velocity dispersion corresponds to a much larger region, typically ~42×76 pc^2 (1.0×1.8 arcsec^2) containing several knots. The use of these wider size scale velocity dispersion measurements to estimate the mass of each knot can lead to an overestimate of the mass of the individual clusters, and hence of each CNSFR (see Paper I).

However, as can be seen in the *HST*–NICMOS image (right-hand panel of Fig. 1), the CNSFRs of NGC 2903 show up very prominently in the NIR and dominate the light inside the apertures observed (see Alonso-Herrero et al. 2001, for a detailed analysis of the IR images). Therefore, the assumption that the light at the CaT wavelength region is dominated by the stars in the clusters seems to be justified. The IR CaT is very strong, in fact the strongest stellar feature in very young clusters, i.e. older than 4 Myr (Terlevich et al. 1990). Besides, we detect a minimum in the velocity dispersion at the position of the clusters (see Fig. 12). Nevertheless, we cannot assert that we are actually measuring their velocity dispersion and thus prefer to say that our measurements of σ_*, and hence dynamical masses, constitute upper limits. Although we are well aware of the difficulties, yet we are confident that these upper limits are valid and important for comparison with the gas kinematic measurements.

Another important fact that can affect the estimated dynamical masses is the presence of binaries among the red supergiant and red giant populations from which we have derived the stellar velocity dispersions. In a recent work, Bosch, Terlevich & Terlevich (2009) using the Gemini Multi-Object Spectrograph (GEMINI–GMOS) data have investigated the presence of binary stars within the ionizing cluster of 30 Doradus. From a seven-epoch observing campaign, they have detected a rate of binary system candidates within their OB star sample of ~50 per cent. Interestingly enough, this detection rate is consistent with a spectroscopic population of 100 per cent binaries, when the observational parameters described in the simulations by Bosch & Meza (2001) are set for their observations. From their final sample of 'single' stars, they estimated a radial velocity dispersion of 8.3 km s^{-1}. When they derived σ_* from a single epoch, they found values as high as 30 km s^{-1}, consistent with the values derived from single epoch New Technology Telescope observations by Bosch et al. (2001).

Although the environment of our CNSFRs is very different from that of 30 Dor and the stellar components of the binary systems studied by Bosch et al. (2009) are very different from the stars present in our regions from where the CaT arises (red supergiants), this is an illustrative observational example of the problem. The orbital motions of the stars in binary (multiple) systems produce an overestimate of the velocity dispersions and hence of the dynamical masses. The single-star assumption introduces a systematic error that depends on the properties of the star cluster and the binary population, with an important effect on the cluster mass if the typical orbital velocity of a binary component is of the order of, or larger than, the velocity dispersion of the single/binary stars in the potential of the cluster (Kouwenhoven & de Grijs 2008). As was pointed out by these authors, the relative weights between the single and binary stars in the velocity dispersion measurements depend on the binary fraction, which, together with the semimajor axis or period distribution, are the most important parameters in order to determine if the binary population affects the estimated dynamical masses. Their simulations indicate that the dynamical mass is overestimated by 70, 50 and 5 per cent for a measured stellar velocity dispersion in the line of sight of 1, 2 and 10 km s^{-1}, respectively. They therefore conclude that most of the known dynamical masses of massive star clusters are only mildly affected by the presence of binaries. Hence, although the binary fraction of the red supergiants and red giants in this type of circumnuclear and typically high metal-rich environment is unknown, for our clusters, where the smallest estimated velocity dispersion is 37 km s^{-1}, we can assume that the contribution of binaries to the stellar velocity dispersions is not important.

7 SUMMARY AND CONCLUSIONS

We have measured gas and stellar velocity dispersions in four CNSFRs and the nucleus of the barred spiral galaxy NGC 2903.

The stellar velocity dispersions have been measured from the CaT lines at λλ 8494, 8542, 8662 Å, while the gas velocity dispersions have been measured by Gaussian fits to the Hβ λ 4861 Å and the [O III] λ 5007Å emission lines on high dispersion spectra.

Stellar velocity dispersions are between 37 and 65 km s^{-1}. These values are about 25 km s^{-1} larger than those measured for the ionized gas from the Hβ emission line using a single-Gaussian fit. On the other hand, single-Gaussian fits to the [O III] 5007 Å line yield velocity dispersions close to the stellar ones, and, in some cases, somewhat larger. However, the best Gaussian fits involved two different components for the gas: a 'broad component' with a velocity dispersion similar to that measured for the stars, and a 'narrow component' with a velocity dispersion lower than the stellar one by about 30 km s^{-1}. This last velocity component shows a relatively constant value for the two gas emission lines, close to 24 km s^{-1} for all the studied CNSFRs (including the regions belonging to NGC 3351 from Paper I). We find a radial velocity shift between the narrow and the broad component of the multi-Gaussian fits in the CNSFRs of NGC 2903 that varies between −10 and 35 km s^{-1}.

When plotted in an [O III]/Hβ versus [N II]/Hα diagram, the two systems are clearly segregated for the high-metallicity regions of NGC 2903, with the narrow component showing lower excitation and being among the lowest excitation line ratios detected within the Sloan Digital Sky Survey data set of starburst systems. Unfortunately, no comparable information exists for the [N II]/Hα ratio, and hence we cannot evaluate any possible contribution by shocks.

The upper limits to the dynamical masses estimated from the stellar velocity dispersion using the virial theorem for the CNSFRs of NGC 2903 are in the range between 6.4×10^7 and 1.9×10^8 M$_\odot$, and is 1.1×10^7 M$_\odot$ for the nuclear region inside 3.8 pc. Masses derived from the Hβ velocity dispersions under the assumption of a single component for the gas would have been underestimated by factors between 2 and 4 approximately. The upper limits to the derived masses for the individual clusters are between 1.4×10^6 and 1.1×10^7 M$_\odot$. These values are between 4.2 and 34 times the mass derived for the SSC A in NGC 1569 by Ho & Filippenko (1996a) and larger than other kinematically derived SSC masses.

Masses of the ionizing stellar clusters of the CNSFRs have been derived from their Hα luminosities under the assumption that the regions are ionization bound and without taking into account any photon absorption by dust. For the star-forming complexes of NGC 2903, these masses are between 1.9 and 2.5×10^6 M$_\odot$, and is 2.1×10^5 M$_\odot$ for the galaxy nucleus. Therefore, the ratio of the ionizing stellar population to the total dynamical mass is between 0.01 and 0.04. These values of the masses of the ionizing stellar clusters of the CNSFRs are comparable to that derived by González-Delgado et al. (1995) for the circumnuclear region A in NGC 7714.

Masses for the ionized gas, also derived from their Hα luminosities, vary between 3.0×10^4 and 7.9×10^5 M$_\odot$ for the star-forming regions, and is 3×10^3 M$_\odot$ for the nucleus of NGC 2903. These values are also comparable to that derived by González-Delgado et al. (1995).

It is interesting to note that, according to our findings, the SSC in CNSFRs seems to contain composite stellar populations. Although the youngest one dominates the ultraviolet light and is responsible for the gas ionization, it constitutes a few per cent of the total mass. This can explain the low EWs of emission lines measured in these regions. This may well apply to other SSC, and therefore conclusions drawn from fits of single stellar population (SSP) models should be taken with caution (e.g. McCrady, Gilbert & Graham 2003; Larsen, Brodie & Hunter 2004). Furthermore, the composite nature of the CNSFRs means that star formation in the rings is a process that has taken place over time periods much longer than those implied by the properties of the ionized gas.

The observed stellar and [O III] radial velocities of NGC 2903 are in good agreement, while the Hβ measurements show shifts similar to those found between the narrow and the broad components. This different behaviour can be explained if the positions of the single-Gaussian fits are dominated by the broad component in the case of the [O III] emission line and by the narrow one in the case of Hβ. The rotation curve corresponding to the slit position through the nucleus shows maximum and minimum values at the positions of the circumnuclear regions, as observed in other galaxies with CNSFRs.

The existence of more than one velocity component in the ionized gas corresponding to kinematically distinct systems deserves further study. Several results derived from the observations of the different emission lines could be affected, among others: the classification of the activity in the central regions of galaxies, the inferences about the nature of the source of ionization, the gas abundance determinations, the number of ionizing photons from a given region and any quantity derived from them. To disentangle the origin of these two components, it will be necessary to map these regions with high spectral and spatial resolution and much better S/N in particular for the O^{2+} lines. High-resolution three-dimensional spectroscopy with Integral Field Units would be the ideal tool to approach this issue.

ACKNOWLEDGMENTS

We acknowledge fruitful discussions with Guillermo Bosch, Nate Bastian and Almudena Alonso-Herrero. We are grateful to Jay Gallagher for a thorough reading of the manuscript and for suggestions that greatly improved its clarity.

The WHT is operated on the island of La Palma by the ING in the Spanish Observatorio del Roque de los Muchachos of the Instituto de Astrofísica de Canarias. We thank the Spanish allocation committee (CAT) for awarding observing time.

Some of the data presented in this paper and used in this work were obtained from the MAST. STScI is operated by the Association of Universities for Research in Astronomy, Inc., under NASA contract NAS5-26555. Support for MAST for non-*HST* data is provided by the NASA Office of Space Science via grant NAG5-7584 and by other grants and contracts.

This research has also made use of the NASA/IPAC Extragalactic Data base (NED) which is operated by the Jet Propulsion Laboratory, California Institute of Technology, under contract with the National Aeronautics and Space Administration and of the SIMBAD data base, operated at the CDS, Strasbourg, France.

This work has been supported by Spanish DGICYT grants AYA-2004-02860-C03 and AYA2007-67965-C03-03. GFH and MVC acknowledge support from the Spanish MEC through FPU grants AP2003-1821 and AP2004-0977. AID acknowledges support from the Spanish MEC through a sabbatical grant PR2006-0049. Furthermore, partial support from the Comunidad de Madrid under grant S-0505/ESP/000237 (ASTROCAM) is acknowledged. Support from the Mexican Research Council (CONACYT) through grant 19847-F is acknowledged by ET and RT. We thank the hospitality of the Institute of Astronomy, Cambridge, where part of this work was developed. GFH and MVC also thank the hospitality of the INAOE, and ET and RT, that of the Universidad Autónoma de Madrid.

REFERENCES

Alonso-Herrero A., Ryder S. D., Knapen J. H., 2001, MNRAS, 322, 757
Athanassoula E., 1992, MNRAS, 259, 328
Begelman M. C., Fabian A. C., 1990, MNRAS, 244, 26P
Benedict G. F., Howell D. A., Jørgensen I., Kenney J. D. P., Smith B. J., 2002, AJ, 123, 1411
Binney J., Tremaine S., 1987, Galactic Dynamics. Princeton Univ. Press, Princeton, NJ, p. 747
Boer B., Schulz H., 1993, A&A, 277, 397
Boily C. M., Lançon A., Deiters S., Heggie D. C., 2005, ApJ, 620, L27
Bosch G., Meza A., 2001, in Aguilar A., Carramiñana A., eds, Rev. Mex. Astron. Astrofis. Conf. Ser. Vol. 11, Observed and Intrinsic Properties of Binary Star Orbits. Instituto de Astronomía, Universidad Nacional Autonóma de México, p. 29
Bosch G., Selman F., Melnick J., Terlevich R., 2001, A&A, 380, 137
Bosch G., Terlevich E., Terlevich R., 2009, AJ, 137, 3437
Bottinelli L., Gouguenheim L., Paturel G., de Vaucouleurs G., 1984, A&AS, 56, 381
Bresolin F., Kennicutt R. C., Jr, 1997, AJ, 113, 975
Bresolin F., Kennicutt R. C., Jr, Garnett D. R., 1999, ApJ, 510, 104
Chu Y.-H., Kennicutt R. C., Jr, 1994, ApJ, 425, 720
Combes F., Gerin M., 1985, A&A, 150, 327
de Vaucouleurs G., de Vaucouleurs A., Corwin H. G., Jr, Buta R. J., Paturel G., Fouque P., 1991, Third Reference Catalogue of Bright Galaxies, Vol. 1–3, XII, 2069 p. 7 figs. Springer-Verlag, Berlin
Díaz A. I., 1988, MNRAS, 231, 57
Díaz A. I., Terlevich E., Pagel B. E. J., Vílchez J. M., Edmunds M. G., 1987, MNRAS, 226, 19
Díaz A. I., Terlevich E., Terlevich R., 1989, MNRAS, 239, 325
Díaz R., Carranza G., Dottori H., Goldes G., 1999, ApJ, 512, 623
Díaz A. I., Álvarez-Álvarez M., Terlevich E., Terlevich R., Portal M. S., Aretxaga I., 2000a, MNRAS, 311, 120
Díaz A. I., Castellanos M., Terlevich E., Luisa García-Vargas M., 2000b, MNRAS, 318, 462
Díaz A. I., Terlevich E., Castellanos M., Hägele G. F., 2007, MNRAS, 382, 251
Dors O. L., Jr., Storchi-Bergmann T., Riffel R. A., Schimdt A. A., 2008, A&A, 482, 59
Fleck J.-J., Boily C. M., Lançon A., Deiters S., 2006, MNRAS, 369, 1392
Friedli D., Benz W., 1995, A&A, 301, 649
García-Vargas M. L., Bressan A., Díaz A. I., 1995, A&AS, 112, 35
González-Delgado R. M. et al., 1994, ApJ, 437, 239
González-Delgado R. M., Pérez E., Díaz A. I., García-Vargas M. L., Terlevich E., Vílchez J. M., 1995, ApJ, 439, 604
Hägele G. F., 2008, PhD thesis, Universidad Autónoma de Madrid
Hägele G. F., Pérez-Montero E., Díaz A. I., Terlevich E., Terlevich R., 2006, MNRAS, 372, 293
Hägele G. F., Díaz A. I., Cardaci M. V., Terlevich E., Terlevich R., 2007, MNRAS, 378, 163 (Paper I)
Hägele G. F., Díaz A. I., Terlevich E., Terlevich R., Pérez-Montero E., Cardaci M. V., 2008, MNRAS, 383, 209
Hägele G. F. et al., 2009, submitted
Haynes M. P., van Zee L., Hogg D. E., Roberts M. S., Maddalena R. J., 1998, AJ, 115, 62
Ho L. C., Filippenko A. V., 1996a, ApJ, 466, L83
Ho L. C., Filippenko A. V., 1996b, ApJ, 472, 600
Homeier N. L., Gallagher J. S., 1999, ApJ, 522, 199
Jarrett T. H., Chester T., Cutri R., Schneider S. E., Huchra J. P., 2003, AJ, 125, 525
Jiménez-Benito L., Díaz A. I., Terlevich R., Terlevich E., 2000, MNRAS, 317, 907
Jogee S., Scoville N., Kenney J. D. P., 2005, ApJ, 630, 837
Kennicutt R. C., Jr., Keel W. C., Blaha C. A., 1989, AJ, 97, 1022
Kouwenhoven M. B. N., de Grijs R., 2008, A&A, 480, 103
Kurtz M. J., Mink D. J., 1998, PASP, 110, 934
Larsen S. S., Brodie J. P., Hunter D. A., 2004, AJ, 128, 2295
Macchetto F., Colina L., Golombek D., Perryman M. A. C., di Serego Alighieri S., 1990, ApJ, 356, 389
McCrady N., Graham J. R., 2007, ApJ, 663, 844
McCrady N., Gilbert A. M., Graham J. R., 2003, ApJ, 596, 240
Maoz D., Barth A. J., Sternberg A., Filippenko A. V., Ho L. C., Macchetto F. D., Rix H.-W., Schneider D. P., 1996, AJ, 111, 2248
Melnick J., Tenorio-Tagle G., Terlevich R., 1999, MNRAS, 302, 677
Mendez D. I., Esteban C., 1997, ApJ, 488, 652
Meurer G. R., Heckman T. M., Leitherer C., Kinney A., Robert C., Garnett D. R., 1995, AJ, 110, 2665
Miller J. S., Mathews W. G., 1972, ApJ, 172, 593
Moll S. L., de Grijs R., Anders P., Crowther P. A., Larsen S. S., Smith L. J., Portegies Zwart S. F., 2008, A&A, 490, 125
Nelson C. H., Whittle M., 1995, ApJS, 99, 67
Östlin G., Cumming R. J., Bergvall N., 2007, A&A, 461, 471
Palacios J., García-Vargas M. L., Díaz A., Terlevich R., Terlevich E., 1997, A&A, 323, 749
Pérez-Olea D., 1996, PhD thesis, Universidad Autónoma de Madrid
Pizzella A., Corsini E. M., Vega Beltrán J. C., Bertola F., 2004, A&A, 424, 447
Planesas P., Colina L., Pérez-Olea D., 1997, A&A, 325, 81
Prada F., Greve A., McKeith C. D., 1994, A&A, 288, 396
Roberts W. W., Jr., Huntley J. M., van Albada G. D., 1979, ApJ, 233, 67
Sakamoto K., Okumura S. K., Ishizuki S., Scoville N. Z., 1999, ApJ, 525, 691
Salpeter E. E., 1955, ApJ, 121, 161
Sheth K., Vogel S. N., Regan M. W., Thornley M. D., Teuben P. J., 2005, ApJ, 632, 217
Sidoli F., Smith L. J., Crowther P. A., 2006, MNRAS, 370, 799
Slavin J. D., Shull J. M., Begelman M. C., 1993, ApJ, 407, 83
Smith L. J., Gallagher J. S., 2001, MNRAS, 326, 1027
Spitzer L., 1987, Dynamical Evolution of Globular Clusters. Princeton Univ. Press, Princeton, NJ, p. 191
Stauffer J. R., 1982, ApJS, 50, 517
Telesco C. M., Decher R., 1988, ApJ, 334, 573
Terlevich E., Terlevich R., Díaz A. I., Pastoriza M. G., Dottori H., 1990, MNRAS, 242, 48P
Terlevich E., Díaz A. I., Terlevich R., González-Delgado R. M., Pérez E., García Vargas M. L., 1996, MNRAS, 279, 1219
Tonry J., Davis M., 1979, AJ, 84, 1511
Tschöke D., Hensler G., Junkes N., 2003, A&A, 411, 41
Westmoquette M. S., Exter K. M., Smith L. J., Gallagher J. S., 2007a, MNRAS, 381, 894
Westmoquette M. S., Smith L. J., Gallagher J. S., Exter K. M., 2007b, MNRAS, 381, 913
Westmoquette M. S., Smith L. J., Gallagher J. S. III, O'Connell R. W., Rosario D. J., de Grijs R., 2007c, ApJ, 671, 358
Westmoquette M. S., Smith L. J., Gallagher J. S., Trancho G., Bastian M., Konstantopoulos I. S., 2009, ApJ, 696, 192

This paper has been typeset from a TEX/LATEX file prepared by the author.